RESEARCH ARTICLE | DECEMBER 05 2024

Effects of upper pier design and geometry on the local scour of skirted caisson with two tandem piers

Special Collection: Flow and Civil Structures

Fang Qiu (裘放) ; Kai Wei (魏凯) ; Ke Tong (童可) ; Zhenchen Hu (胡振晨) ; Changrong Yao (姚昌荣) ; Jingxi Qin (秦竟熙)

Physics of Fluids 36, 125139 (2024)
https://doi.org/10.1063/5.0235791

Physics of Fluids ARTICLE pubs.aip.org/aip/pof

Effects of upper pier design and geometry on the local scour of skirted caisson with two tandem piers

Cite as: Phys. Fluids **36**, 125139 (2024); doi: 10.1063/5.0235791
Submitted: 29 August 2024 · Accepted: 7 November 2024 ·
Published Online: 5 December 2024

View Online Export Citation CrossMark

Fang Qiu (裘放),[1] Kai Wei (魏凯),[1,a)] Ke Tong (童可),[2] Zhenchen Hu (胡振晨),[2] Changrong Yao (姚昌荣),[2] and Jingxi Qin (秦竟熙)[3]

AFFILIATIONS

[1]State Key Laboratory of Bridge Intelligent and Green Construction, Southwest Jiaotong University, Chengdu 611756, Sichuan, China
[2]Department of Bridge Engineering, Southwest Jiaotong University, Chengdu 610031, Sichuan, China
[3]Department of Civil and Environmental Engineering, The HongKong Polytechnic University, Hong Kong, China

Note: This paper is part of the special topic, Flow and Civil Structures.
[a)]**Author to whom correspondence should be addressed:** kaiwei@home.swjtu.edu.cn

ABSTRACT

Local scour induced by strong currents has become one of the major challenges for sea-crossing bridges built for the convenience of transportation across bays. To mitigate the local scour of the sea-crossing bridge foundation, this study optimized the design and geometry of the upper part of the skirted caisson and proposed a new type of foundation called the skirted caisson with two tandem piers (SCTTP). Systematic experimental and numerical investigations into the influence of the design parameters of SCTTPs on scour protection were conducted, and the temporal development and mechanism of local scour in SCTTPs were investigated. The following conclusions can be drawn: (1) although the scour of the SCTTP is slightly greater than that of the skirted caisson, the scour terrain of the SCTTP is more stable; (2) the scour of the SCTTP with circular piers is small, and the flat surfaces of semicircular-ended and square piers can intensify the scour; (3) the scour at the front and back of the SCTTP gradually becomes independent of the distance between the two piers, causing the total scour of the SCTTP to increase; and (4) as the width of the tie beam decreases, the scour of the SCTTP with the groove becomes more significant than that of the SCTTP with no groove, but the groove depth has little effect on the maximum scour depth of the SCTTP with the groove. These findings provide insight into the design optimization of SCTTPs from scour.

I. INTRODUCTION

To fulfill the growth of the economic development of coastal landscapes, many sea-crossing bridges have been built for the convenience of transportation across bays,[1] straits, and waterways, such as Hangzhou Bay Bridge,[2] Hong Kong-Zhuhai-Macao Bridge, and Donghai Bridge.[3] According to the reports of Li *et al.*[4] and Liu *et al.*,[5] the maximum current velocity at the 300-year return period is 5.30 m/s for the site of Hangzhou Bay Bridge and 3.47 m/s at Xihoumen Rail-cum-Road Bridge, which is even larger than the design flow velocity of bridges in the Yangtze River.[6] The local scour induced by strong currents has become one of the major challenges for sea-crossing bridges in strait waterways.[7] For example, the maximum scour depth of the Donghai Bridge has increased by 8.7 m after five years of operation and has already approached the warning scour line for structural safety.[8] Therefore, it is important to comprehensively consider scour mitigation in the structural design of foundations for sea-crossing bridges.

Over the past decades, a large number of scholars have researched scour countermeasures to resist and reduce local scour on foundations, mainly consisting of passive and active countermeasures. Ripraps are the most popular passive countermeasures due to their low cost and accessible collection.[9] The particle size of the riprap[10,11] and the position arrangement[12] around the foundation affect the optimum effect of scour resistance, which comes into play in failure mechanism research.[13] In addition to riprap, gabion,[14] sludge solidification,[15] geotextile,[16] and so on have been investigated experimentally and numerically by scholars. However, these other passive countermeasures are less commonly used in practical engineering. In addition, various active countermeasures have been studied experimentally and numerically to reduce the scour depth, such as sacrificial piles,[17,18] collars,[19,20]

submerged vanes,[21,22] and bed sills.[23,24] These active countermeasures decrease the scour depth by altering and reducing the incoming flow intensity. However, active countermeasures are also less commonly used in practical engineering. The reason is that the scour countermeasures mentioned above are adjuncts to foundation structures. The life of scour countermeasures is much shorter than that of foundation structures and requires long-term maintenance, which requires significantly more labor and money.

Integrating protection and structure is more convenient for construction and maintenance compared with the scour countermeasures of the adjuncts. Qin *et al.*[25] proposed a skirted caisson (formed by shrinking the upper volume of the uniform caisson). Compared with the uniform caisson, the skirted caisson has a lighter self-weight. Moreover, skirts can reduce the scour depth of skirted caissons. Both self-weight and local scour reduction can reduce the embedment depth of the caisson bottom, reducing construction costs. Wei *et al.*[26] investigated the effect of the design parameters of skirted caissons on local scour experimentally and numerically and revealed the scour development law and mechanism of skirted caissons under different design parameters. Xu *et al.*[27] studied the influence of skirt elevation on local scour experimentally and found that when the embedment depth of the skirt is equal to 0.6 and 0.81 times the water depth, the maximum scour depth is reduced by 18.8% and 19.9%, respectively. Hu[28] provided the following design scheme for a skirted caisson: the skirt width is 9–10 m, the skirt elevation is -0.6 times the water depth, and the height of the hook above the skirt is 0.15 times the water depth, which can yield a small scour depth. In short, skirted caissons have great advantages in scour protection.

However, with the construction of wide sea-crossing bridges,[29] the aspect ratio of the foundation gradually increases, which causes the negative effects of the upper part of the skirted caisson to increase in terms of hydrodynamic performance and esthetics. Therefore, this study optimized the design and geometry of the upper part of the skirted caisson, and a new type of foundation called the "SCTTP" was proposed, which is formed by replacing the upper round-ended pier with two tandem small piers, as shown in Fig. 1. The SCTTP further reduces the self-weight of the skirted caisson, which can further reduce the consumption of building materials and the embedment depth of the caisson. In addition, the volume of the pier is significantly reduced compared with that of the upper skirted caisson. Therefore, piers can be prefabricated in factories and installed integrally on the scene. The construction efficiency will be significantly improved, and the construction time will be greatly reduced, which is essential for the construction of coastal bridges.

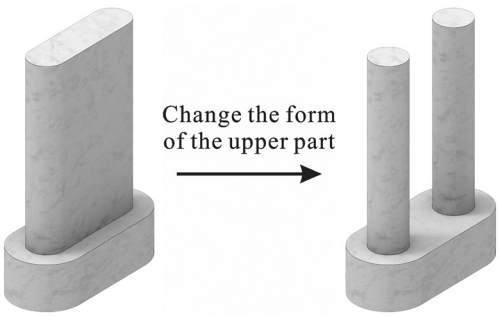

FIG. 1. Proposal of the SCTTP.

Nevertheless, investigations of local scours on SCTTPs have not yet been performed, and previous studies have focused on the local scours of the components of SCTTPs, such as single piers, two tandem piers, and uniform caissons. For the single pier, Sharp and McAlpin[30] experimentally investigated the effect of pier nose extensions on the local scour of a nontypical pier and reported that pier nose extensions produced a local scour reduction of 53% compared with piers without extensions. Li *et al.*[31] conducted scour protection experiments around monopile using the microbial induced carbonate precipitation and reported that the maximum scour depth was reduced by 84% after 2-times treatments. Li *et al.*[32] numerically studied the influence of a spoiler structure for scour protection and reported that the novel spoiler structure shows promising results for local erosion protection. Guan *et al.*[33] investigated three machine learning algorithms for predicting the local scour depth around pile foundations and conducted a sensitivity analysis of the variables and reported that the SVM model has higher accuracy and that the ratio of velocities is the most effective parameter. Wang *et al.*[34] studied the effect of scour remediation by solidified soil on the lateral response of monopiles and provided insights into the mechanisms of how solidified soil affects the lateral bearing capacity of monopiles under different conditions. Barrie *et al.*[35] investigated the mechanism of local scour around pile under sloping bed conditions and reported that the scour depth increased significantly in sloped scenarios and that negative slopes intensified the scour process due to higher hydrodynamic forces. For the tandem piers, Wang *et al.*[36] experimentally investigated the effect of pier spacing on the local scour of upstream and downstream piers and reported that the local scour depth of the downstream pier gradually increases with increasing pier spacing due to the weakened sheltering effect of the upstream pier. Yu *et al.*[37] numerically studied the local scour of tandem piers and proposed a shielding coefficient for calculating the scour depth. Qi *et al.*[38] numerically explored the effects of the span and the collar on the characteristics of the local scouring behavior around two tandem piers and proposed an optimization scheme to achieve an economic protective effect by reducing the collar size of the downstream pier. For caissons, Zhao *et al.*[39] investigated the effect of incident directions of the flow on the local scour under a smaller ratio of the caisson height to width and reported that the horseshoe vortex plays a far lesser role than the velocity amplification at the corners of the caisson. Xiang *et al.*[40] studied the local scour induced by unidirectional and tidal currents around caissons with different cross sections and reported that the effect of current type can significantly influence the size and location of the maximum scour depth around circular and square caissons.

Although the local scour of the components of SCTTP has been extensively studied, the overall structure of SCTTP has not been investigated. The additional design parameters are generated when the skirted caisson is transformed into the SCTTP, and the effects of these SCTTP parameters on local scour are still unclear. Therefore, in this paper, systematic experimental and numerical investigations of the design parameters of SCTTP for scour protection were carried out. First, scour experiments of nine SCTTP models were conducted, and the scour depths around the models and scour terrain photographs at the moment of 24-h scour were obtained. Additionally, the scour terrain was reconstructed using oblique photogrammetry technology.

Second, numerical simulations under the test terrain were carried out, and the flow field of the nine SCTTPs was obtained. Third, the scour depth and scour terrain from tests and the streamlines, vortexes, and shear from numerical simulations were discussed. The law and mechanism of local scour of SCTTPs with different design parameters were revealed. Finally, the major conclusions of this work are discussed, and future research prospects are proposed.

II. EXPERIMENTAL SETUP

A series of experiments were carried out in the current flume with a length of 20 m, width of 1 m, and height of 0.7 m, as illustrated in Fig. 2. There is a 4 m long, 1 m wide, and 0.5 m deep sand pool in the middle of the flume for the local scour tests. There are three sliding racks above the sand pool to fix the acoustic Doppler velocimeter (ADV), the test model, and the other devices. The height of the lifter on the middle sliding rack can be adjusted. The water flows from the left inlet to the right outlet. The pump draws water from the impounding reservoir to control the inlet flow rate, and the baffle height controls the outlet flow rate to obtain the desired water depth and flow velocity through the above adjustment methods. The grille screens can reduce the turbulent kinetic energy of the inlet flow to ensure flow stability in the test section.

A. Models and testing devices

A sketch of the SCTTP is shown in Fig. 3. The primary design parameters of the SCTTP include the cross-sectional shape of the pier, the distance between two piers l, the width of the tie beam b, the skirt width w, the skirt elevation h (the distance between the skirt top surface and the riverbed surface. In this paper, the skirted elevation is equal to 0, which indicates that the skirt top surface is located just at the riverbed surface; the skirt elevation is not marked in Fig. 3), and the skirt form. Notably, this paper mainly studies the first three parameters, as the parameters w, h, and skirt form have been investigated in the authors' previous work.[26] l refers to the distance between the centers of the piers. b is the distance between the two sides of the tie beam boundary. When b is less than D, the shape of the skirt changes from a round-ended shape to a dumbbell shape.

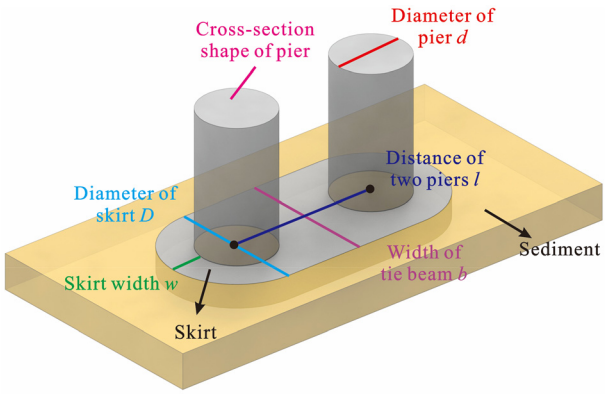

FIG. 3. Sketch and design parameters of the SCTTP model.

In this study, nine models were built to investigate the local scour performance of SCTTPs, including seven SCTTPs, one uniform caisson (a column-type structure with a uniform cross section), and one skirted caisson (a caisson with a small upper round-ended section depending on the bridge pylon's arrangement and the superstructure's force transfer). This paper assumes that the above requirements can be met when the length and width of the pier are set to d ($d = 4$ cm). In addition, the other parameters of the SCTTP are normalized to d for convenience and universality. In this paper, the diameter of the skirt D is equal to $2\,d$, the skirt width w is equal to $0.5\,d$, and the skirt elevation h is set to 0. For the uniform caisson, the cross section is a round-ended shape, similar to the section of the SCTTP skirt, the length of the uniform caisson is equal to $4.5\,d$, and the width is equal to $2\,d$. For the skirted caisson, the upper and lower cross sections are round-ended shapes,

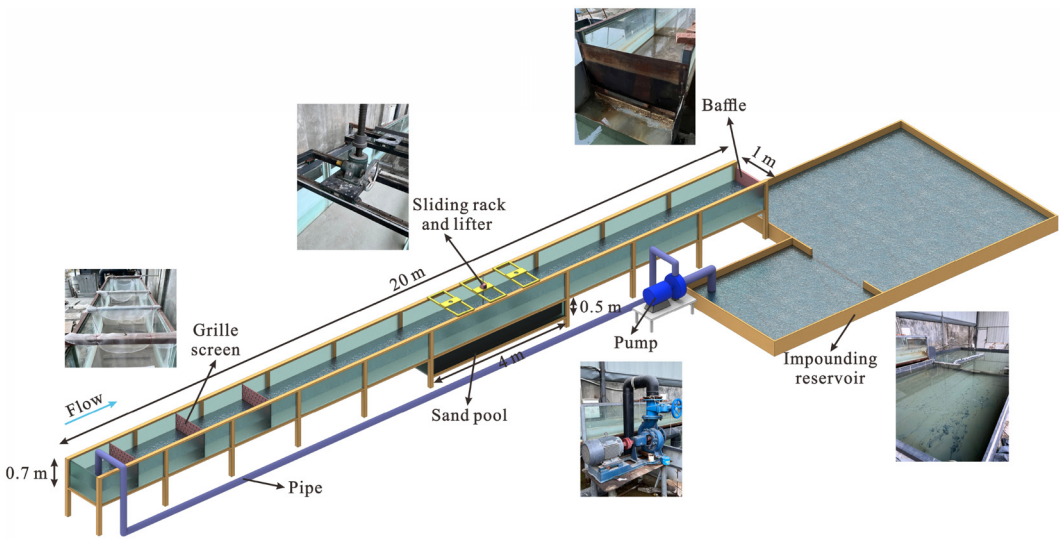

FIG. 2. Details of the experimental flume.

TABLE I. Design parameters of the models.

Model	w	h	The cross-sectional shape of the pier	l	b	D	Form
#1	...	...	...	2.5 d	2 d	2 d	Uniform caisson
#2	0.5 d	0	Round-end	...	2 d	2 d	Skirted caisson
#3	0.5 d	0	Circular	2.5 d	2 d	2 d	Round-ended skirt
#4	0.5 d	0	Semicircular-ended	2.5 d	2 d	2 d	Round-ended skirt
#5	0.5 d	0	Square	2.5 d	2 d	2 d	Round-ended skirt
#6	0.5 d	0	Circular	1.5 d	2 d	2 d	Round-ended skirt
#7	0.5 d	0	Circular	3.5 d	2 d	2 d	Round-ended skirt
#8	0.5 d	0	Circular	2.5 d	1.5 d	2 d	Dumbbell skirt
#9	0.5 d	0	Circular	2.5 d	d	2 d	Dumbbell skirt

and the skirt width is 0.5 d. The investigated parameters of the SCTTPs include three foundation forms (uniform caisson, skirted caisson, and SCTTP), three pier cross-sectional shapes (circular, semicircular-ended, and square), three pier distances (1.5 d, 2.5 d, and 3.5 d), and three tie beam widths (2 d, 1.5 d, and d). The detailed parameters of the models are listed in Table I. Additionally, the blockage ratio of the model's maximum width to the flume width is smaller than the critical blockage ratio of 1/9 when the inflow direction is equal to 0°,[41] which can reduce the influence of the flume boundary on the flow field around the models.

The test models of the bridge foundation were made of acrylic materials. The thickness of the acrylic shell was 0.5 cm. Vertical rulers were installed around the models' monitoring points to observe the scour depth during the tests. The number of vertical rulers varied with the test models. Eight vertical rulers were installed on the pier, twelve on the round-ended skirt and the upper part of the skirted caisson and uniform caisson, and sixteen on the dumbbell skirt, as shown in Fig. 4.

An underwater camera was used during the tests to record the scour depth at the monitoring points, as shown in Fig. 5. It is well known that scour develops rapidly in the initial stage, after which the rate of scour development gradually decreases. The following measurement method was adopted to accurately determine the local scour depth during the scour development process. During the first hour of the test, local scour depth measurements were taken every 15 min; during the second hour, measurements were taken every 30 min; during the third and fourth hours, measurements were taken every 60 min; and after the fourth hour, measurements were taken every 120 min.

The flow velocity was measured by an ADV, as shown in Fig. 6. Before the scour tests, the ADV acquired the velocity profile at the installation location of the model. The distribution of the measuring points along the direction of the water depth is dense near the riverbed and sparse near the water surface for a more accurate velocity profile. Additionally, the measurement frequency is 100 Hz, and the measurement time of each measuring point is 3 min. The flow velocity at the measurement point is taken as the average flow velocity within 3 min.

After the tests, the scour terrain data were collected by oblique photogrammetry technology, which is an urban spatial information collection and stereo mapping method.[42,43] Oblique photogrammetry technology includes three basic procedures,[44–46] the basic principles of which can be described as follows:

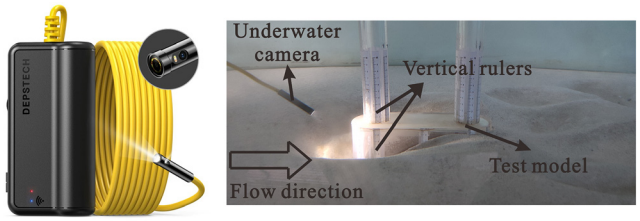

FIG. 5. Local scour depth measurement device and process: (a) underwater camera and (b) local scour depth measurement at the monitoring points.

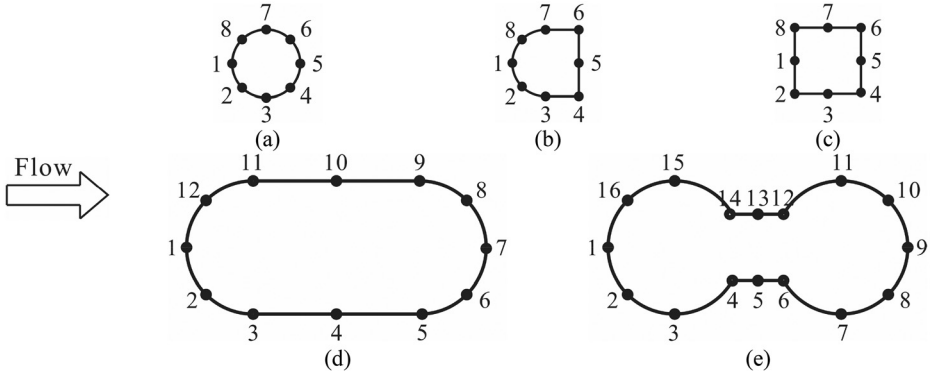

FIG. 4. Distribution of monitoring points for different parts of the test models: (a) circular pier, (b) semicircular-ended pier, (c) square pier, (d) round-ended skirt/uniform caisson, and (e) dumbbell skirt.

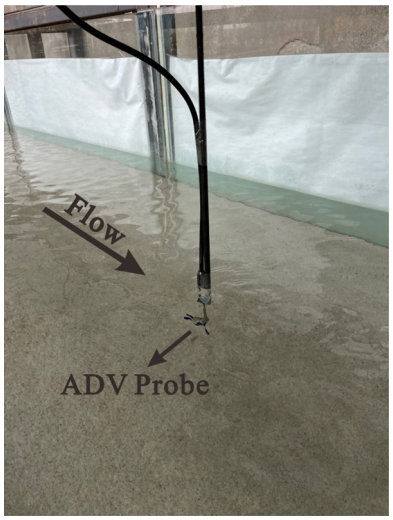

FIG. 6. Flow velocity measurement via ADV.

Step 1: Acquire topographic photographs. The photographs can be obtained through fixed cameras or cameras carried by drones. The photographs should cover a full 360-degree view of the angle, as shown in Fig. 7(a), and the image overlap of two adjacent photographs cannot be less than 60%.

Step 2: Joint adjustment of images. The control points in each image, as shown in Fig. 7(b), are set, the 3D space network is calculated and adjusted using the aerial triangulation method, and the coordinate information of a large number of image points from different photographs is obtained.

Step 3: Calculate the point cloud network. The point clouds of all the images are calculated and connected to form a network, and finally, the 3D point cloud coordinate model of the terrain is obtained, as shown in Fig. 7(c).

Steps 2 and 3 can be processed by importing the photographs into the three-dimensional (3D) reconstruction software ContextCapture to construct the 3D numerical terrain model.[47] Compared with the traditional ruler measuring method, oblique photogrammetry technology is much faster and includes a larger terrain range. The measurement accuracy can be evaluated by comparing the feature point coordinates or feature dimensions of the target object and the model.[48–51] Figure 8 compares the scour terrain of the test model with that of the reconstructed model. Compared with that of the traditional ruler measurement method, the reconstructed maximum scour depth error is less than 7% for all the cases, which indicates that oblique photogrammetry technology is acceptable and efficient for scour terrain measurement.

B. Sediment and flow conditions

The measured density of the quartz sand used in this study was 2690 kg/m^3, which has a uniform grading curve with a median grain size, d_{50}, of 0.3062 mm and a geometric standard deviation, σ_g, of 1.31 (calculated from $\sqrt{d_{84}/d_{16}}$), as shown in Fig. 9.

The water depth is constrained by two indicators: the ratio of the model width to the water depth and the flume width to the water depth. The ratio of the model width to the water depth should be less than 0.7[52] to avoid interactions between the horseshoe vortex and the backwater. The ratio of the flume width to the water depth should be larger than 5[53] to reduce the effect of secondary flow on the model. The maximum width of the model is 0.08 m, and the flume width is 1 m. Therefore, the water depth ranges from 0.114 to 0.2 m. In this paper, the water depth is set to 0.195 m for all the testing cases.

A clear-water scour test was conducted to investigate the scour performance of the SCTTP. The critical velocity of the sediment calculated by HEC-18,[54] which has high precision for scour depth prediction,[55,56] is 0.3177 m/s. Hence, the test flow velocity is set to 0.26 m/s, which is lower than the calculated critical velocity to ensure clear-water conditions.

C. Determination of scour duration

In this study, the focus of the experimental program is to understand the change of local scour as a function of caisson design and geometry. It would undoubtedly have been better to carry out all of the tests to a convincing equilibrium. Melville and Chiew[57] and Mia and Nago[58] reported that equilibrium scour was achieved when the scour depth increased by no more than 5% of the pier diameter in 24 h. Cardoso and Bettess[59] noted that scour will reach an equilibrium state when the slope of the scour depth vs the logarithm of time approaches zero. According to these indicators, each test may require one more week, which is time-consuming for a parametric study with multiple tests. Considering that this study does not propose a formula for predicting equilibrium values, the duration of all nine scour tests is set to 24 h for a balance between efficiency and budget.

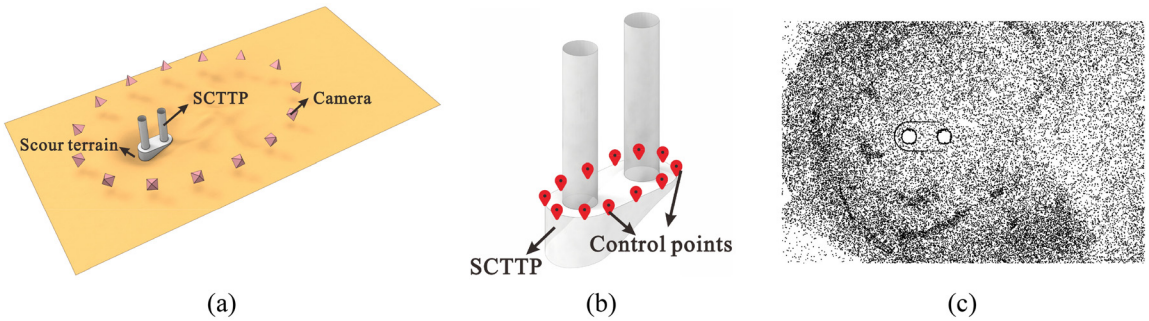

FIG. 7. Process of oblique photogrammetry: (a) take 360-degree photographs of scour terrain, (b) set control points, and (c) point cloud of scour terrain.

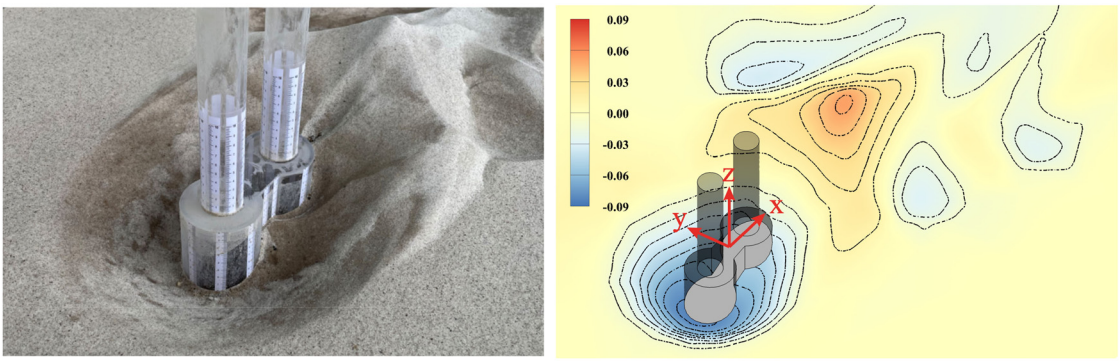

(a) (b)

FIG. 8. Comparison of scour terrains between the test model and reconstructed model: (a) test photograph of the scour terrain and (b) scour terrain reconstructed by oblique photogrammetry technology.

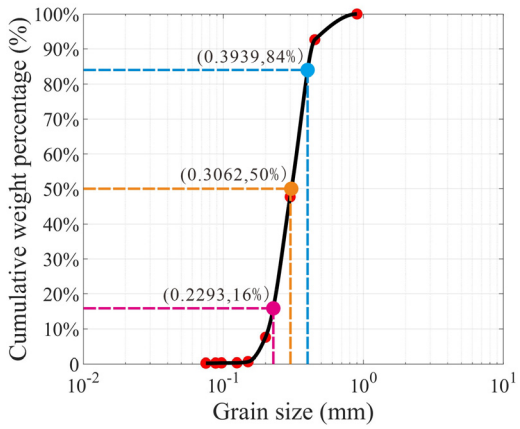

FIG. 9. Grading curve of the test sediments.

Some researchers have attempted to estimate the equilibrium scour depth based on tests with finite time.[60–62] Yang *et al.*[63] proposed a function to extrapolate experimental temporal scour data to achieve the equilibrium scour depth as follows:

$$d_s(t_s) = p_1[1-\exp(-p_2 t_s)] + p_3[1-\exp(-p_4 t_s)] + p_5[1-\exp(-p_6 t_s)] + p_7[1-\exp(-p_8 t_s)] + p_9[1-\exp(-p_{10} t_s)], \quad (1)$$

in which d_s is the scour depth, t_s is the scour testing time, and p_i represents the fitting coefficient, which can be fitted by the least squares method from existing scour test data. According to the equation, the fitting equilibrium scour depth, d_{se}, is equal to $p_1 + p_3 + p_5 + p_7 + p_9$ when the time is set to infinity.

To estimate the relationship between the 24-h scour depth and the equilibrium scour depth, Eq. (1) was utilized to fit and extrapolate the experimental scour depth. Figure 10 illustrates the experimental data and the fitting curve of the development of the maximum scour depth for all the models. The fitting equilibrium scour depth obtained from the fitting curve is also marked on the corresponding figure by the horizontal dashed line. The fitting results were satisfactory, and the 24-h scour depth was close to the equilibrium scour depth. Table II presents the fitting coefficients of Eq. (1) for each fitting curve and compares the 24-h scour depth and the fitting equilibrium scour depth. According to the estimation using Eq. (1), the 24-h scour depth can reach 94%–97% of the fitting equilibrium scour depth.

D. The procedure of scour tests

(1) Preparatory phase: fill and level the sand pool with uniform quartz sand and lower the baffle height until the outlet is blocked entirely. The pump was started, and water was slowly added to the flume. The sediment was gradually soaked while adding water, but no scour occurred, and the water depth gradually increased. When the water depth reached a certain height (this height of the water protected the riverbed from scour by the surging water), the pump power and the baffle height were adjusted until the water depth and the flow velocity satisfied the test conditions, and the pump power and the baffle height were recorded.
(2) Setup phase: install the test model, level the riverbed and lower the baffle again. The addition of water from the first step was repeated to ensure that no scour occurred. When the water depth reached a certain height, the pump power and baffle height were adjusted to the recorded values, and the scour test began.
(3) Testing phase: during the test, the scour depth of the monitoring points around the model was collected using an underwater camera. After the test, the pump was switched off, and the water was allowed to drain out and seep down until the sand surface dried. The scour terrain information was subsequently collected, and 360-degree photographs of the scour terrain were taken.

III. NUMERICAL INVESTIGATION INTO FLOW AROUND SCTTP

A. Description of the numerical method

The RANS equations close to the RNG $k-\varepsilon$ turbulence model are adopted as the governing equations for the incompressible viscous

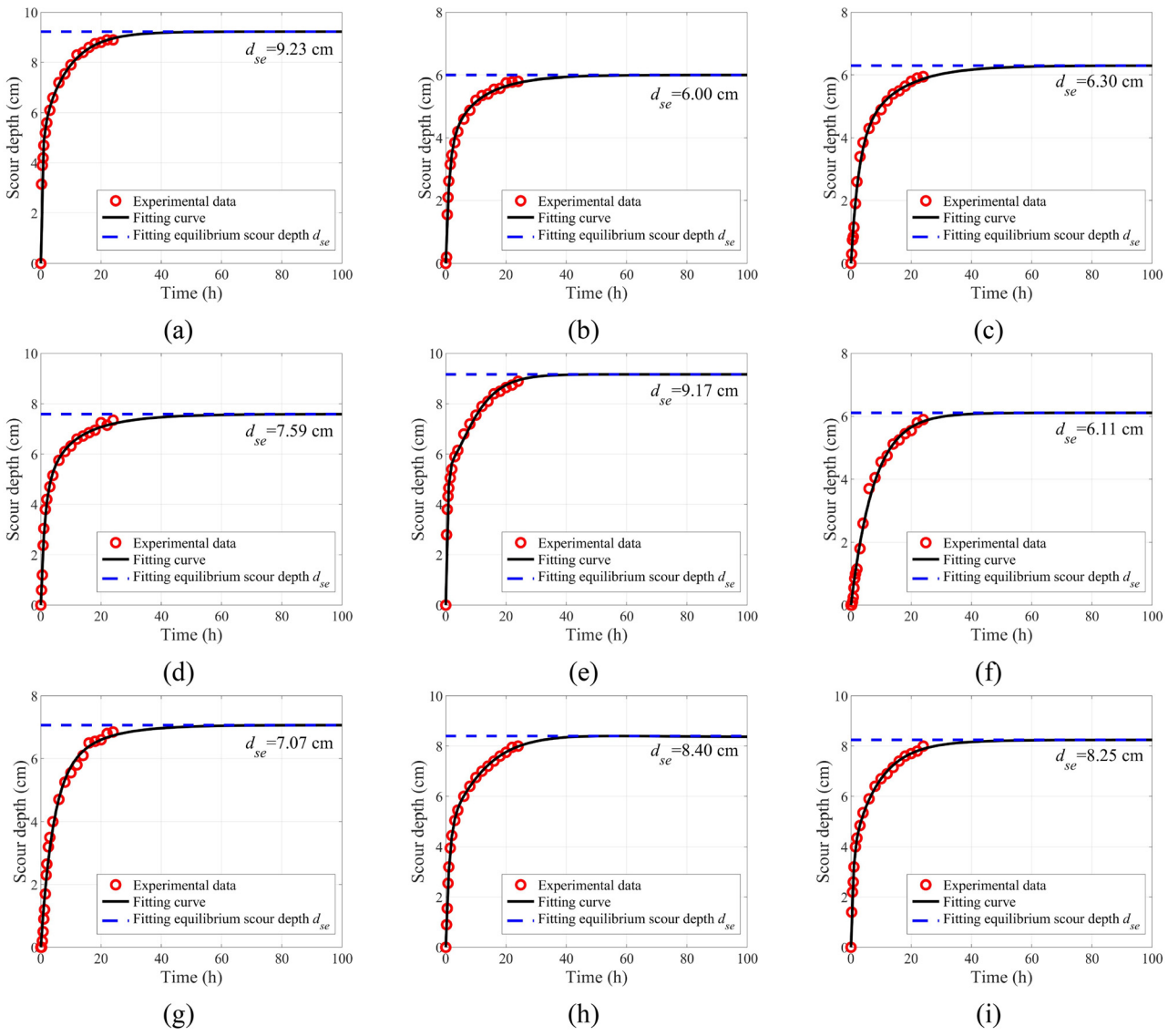

FIG. 10. The experimental data and the fitting curve of the development of the maximum scour depth for all the models: (a) model #1, (b) model #2, (c) model #3, (d) model #4, (e) model #5, (f) model #6, (g) model #7, (h) model #8, and (i) model #9.

fluid motion around the skirted caisson. The governing equations of RANS are expressed as

$$\frac{\partial \rho}{\partial t} + \frac{\partial}{\partial x_i}(\rho u_i) = 0, \tag{2}$$

$$\frac{\partial}{\partial t}(\rho u_i) + \frac{\partial}{\partial x_j}(\rho u_i u_j) = -\frac{\partial p}{\partial x_i} + \frac{\partial}{\partial x_j}\left[\mu\left(\frac{\partial u_i}{\partial x_j} + \frac{\partial u_j}{\partial x_i} - \frac{2}{3}\delta_{ij}\frac{\partial u_l}{\partial x_l}\right)\right] + \frac{\partial}{\partial x_j}\left(-\rho\overline{u_i' u_j'}\right), \tag{3}$$

where ρ is the density of water, t is the time, x_i and x_j are the coordinate axes, u_i, u_j, and u_l are the velocity components, p is the total pressure, δ_{ij} is the Kronecker delta, and u_i and u_i' are the mean and fluctuation water velocities, respectively.

The RNG $k-\varepsilon$ turbulence model is as follows:

$$\frac{\partial}{\partial t}(\rho k) + \frac{\partial}{\partial x_i}(\rho k u_i) = \frac{\partial}{\partial x_j}\left(\alpha_k \mu_{eff}\frac{\partial k}{\partial x_j}\right) + G_k + G_b + \rho\varepsilon + S_k, \tag{4}$$

$$\frac{\partial}{\partial t}(\rho \varepsilon) + \frac{\partial}{\partial x_i}(\rho \varepsilon u_i) = \frac{\partial}{\partial x_j}\left(\alpha_\varepsilon \mu_{eff}\frac{\partial \varepsilon}{\partial x_j}\right) + C_{1\varepsilon}\frac{\varepsilon}{k}(G_k + C_{3\varepsilon}G_b) - C_{2\varepsilon}\rho\frac{\varepsilon^2}{k} - R_\varepsilon + S_\varepsilon, \tag{5}$$

TABLE II. Fitting coefficients and comparison of the 24-h scour depth and the fitting equilibrium scour depth.

Model	#1	#2	#3	#4	#5	#6	#7	#8	#9
p_1	−49.26	0.62	−0.70	0.79	−1.86	0.29	2.02	23.98	0.56
p_2	1.18	0.27	0.27	0.13	0.44	1.68	0.07	0.13	0.84
p_3	−1.67	1.59	1.11	1.50	−4.94	2.44	−2.48	4.64	25.43
p_4	0.76	0.35	0.51	0.13	0.06	1.49	0.27	1.67	0.90
p_5	6.41	3.09	2.44	1.80	9.11	4.12	3.65	−5.88	0.88
p_6	2.45	0.21	0.07	0.13	0.07	0.12	0.91	0.26	0.33
p_7	4.13	−0.01	2.87	0.64	5.91	0.52	1.85	1.20	1.95
p_8	0.11	0.64	0.32	0.13	0.81	0.06	0.32	2.20	0.09
p_9	49.61	1.77	0.58	1.38	0.14	0.89	2.55	−14.76	−22.83
p_{10}	1.13	0.07	0.45	0.13	0.49	1.43	0.23	0.13	0.88
r^2	0.99	0.99	1.00	0.99	0.99	0.99	0.99	1.00	1.00
24-h scour depth d_{s_24} (cm)	8.90	5.80	5.95	7.35	8.90	5.90	6.85	8.00	8.00
Fitting equilibrium scour depth d_{se} (cm)	9.23	6.00	6.30	7.59	9.17	6.11	7.07	8.40	8.25
d_{s_24}/d_{se}	0.96	0.97	0.94	0.97	0.97	0.97	0.97	0.95	0.97

where k is the turbulent kinetic energy, ε is the turbulent dissipation rate, u_i is the velocity component, α_k and α_ε are the inverse effective Prandtl numbers for k and ε, respectively, μ_{eff} is the effective viscosity, G_k is the generation of turbulent kinetic energy due to the mean velocity gradients and can be calculated by $G_k = \mu_t(\partial u/\partial z)^2$ based on the Boussinesq assumption, G_b is the generation of turbulent kinetic energy due to buoyancy, S_k and S_ε are user-defined source terms, and $C_{1\varepsilon}$, $C_{2\varepsilon}$, and $C_{3\varepsilon}$ are turbulent model constants. The factor $R_\varepsilon = \frac{C_\mu \rho \eta^3 (1-\eta/\eta_0)}{1+\beta\eta^3}\frac{\varepsilon^2}{k}$, where $C_\mu = 0.0845$, $\eta = S_k/\varepsilon$, $\eta_0 = 4.38$, and $\beta = 0.012$.

B. Numerical flume modeling considering scour terrain

In this investigation, Fluent, a commercial software package, was employed to explore the intricacies of local scour mechanisms. The 3D CFD numerical flume was configured in such a way that the width and water depth were the same as those in the physical experiment. In contrast, the length of the numerical flume was decreased to 50 times the length of the skirt ($l + D$) to optimize the computational efficiency, as shown in Fig. 11. The inlet of the flume is 35 ($l + D$) from the center of the SCTTP, which allows the flow to develop fully. The outlet is 15 ($l + D$) from the center of the SCTTP, and this distance is sufficient for developing the wake vortex. Additionally, the terrain of the numerical flume was divided into three parts (flat terrain, scour terrain, and flat terrain) along the flow direction. The terrain in front of the scour terrain was flat, which was consistent with the results of the clear-water scour test. The length of the scour terrain was 2 m, which covered the central part of the scour hole, and the front and back of the scour terrain were 0.6 and 1.4 m from the center of the SCTTP, respectively. The terrain behind the scour terrain was not flat in the experiment, whereas the fluctuation degree of the terrain was small and had little influence on the flow field around the SCTTP. Therefore, the terrain behind the scour terrain was simplified into flat terrain. Since the terrain length was 50 times the length of the skirt, the length of the two flat terrains was uncertain and varied with the length of the skirt.

Notably, the numerical research in this paper focuses on the flow field after scour rather than the further development of scour. Therefore, the experimental scour terrain as a wall boundary was imported into Fluent for the flow field calculation. For convenience of description, a Cartesian coordinate system is established, and the point of origin is set in the center of the skirt surface, indicating that the flat riverbed elevation is 0.

The boundary conditions (BCs) for the computational domain are shown in Fig. 12. The flow inlet was set as the velocity BC, and the

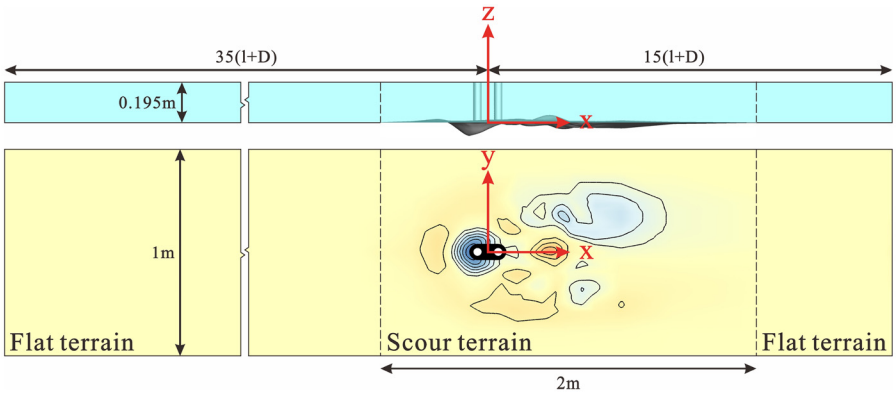

FIG. 11. Map of the numerical flume with scour terrain.

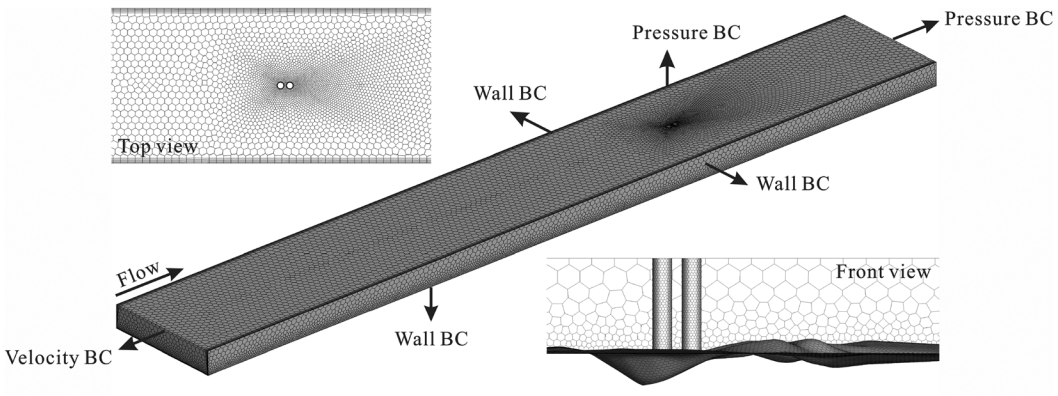

FIG. 12. Mesh of the 3D numerical flume.

flow velocity was equal to the test velocity of 0.26 m/s. The outlet and top boundaries were set as pressure BC to ensure water outflow and simulate the actual atmospheric boundary. The two sides of the numerical flume and the SCTTP were set as the no-slip wall BCs. The bottom boundary was set as the wall BC with a constant roughness height of d_{50} to simulate the riverbed, which is a method widely used in scour simulations.[64–66]

This study used an unstructured polygrid to divide the fluid domain, as shown in Fig. 12. Fine grids were applied around the SCTTP and riverbed to capture the contour features of the SCTTP and the undulating riverbed more precisely. Coarse grids were adopted in other regions to improve the computational efficiency. Additionally, the boundary layer grid was set around the wall BCs, and five layers of boundary layer grids were set on the boundary of the SCTTP and the boundaries of the two sides and bottom of the numerical flume. The first layer height was 5 mm, and the calculated y+ fell between 30 and 100, which met the requirements of the $k-\varepsilon$ turbulence model.

C. Grid independence test

The grid resolution plays an essential role in the calculation results. The simulation accuracy increases as the grid resolution increases. However, increasing the simulation accuracy by increasing the grid density is impractical due to the computational expense. The grid independence test is critical for balancing the simulation accuracy and efficiency. Model #3 was used to evaluate the mesh quality, which did not change significantly when the change in structural form was localized.[67,68] In this study, the maximum change size of the model accounts for 0.4% and 4% of the length and width of the numerical flume, respectively, which has a smaller effect on the flow field when the boundary conditions, initial conditions, and mesh generation methods are the same. Three grid resolutions, namely, "coarse," "medium," and "refined", were tested under the same flow conditions with a velocity of 0.26 m/s and a water depth of 0.195 m, as shown in Fig. 13. The maximum grid size and grid number for the "coarse," "medium," and "refined" meshes were (0.073 m, 500 328), (0.05 m, 1 006 869), and (0.036 m, 2 001 213), respectively.

The velocity profiles at various positions around SCTTP Model #3 [at distances of $-2.5(l+D)$, $-3.25\,D$, and $2.5(l+D)$ from the model center] were simulated using different grid resolutions and are depicted in Fig. 14. The velocity variance between the medium and refined grids is smaller than that between the coarse and medium grids, especially the flow velocity at the back of the SCTTP.

The grid convergence index (GCI) is applied to evaluate the numerical calculation errors caused by the grid resolution and can be calculated by

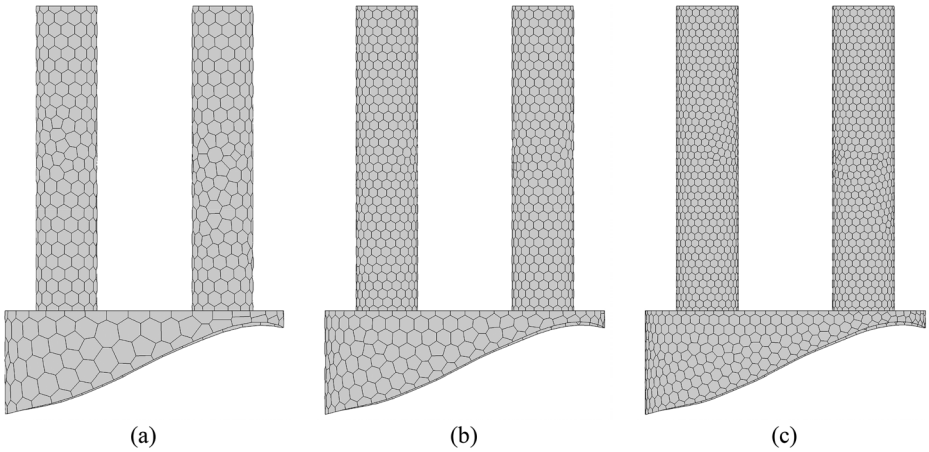

FIG. 13. The three grid resolutions: (a) coarse grid, (b) medium grid, and (c) refined grid.

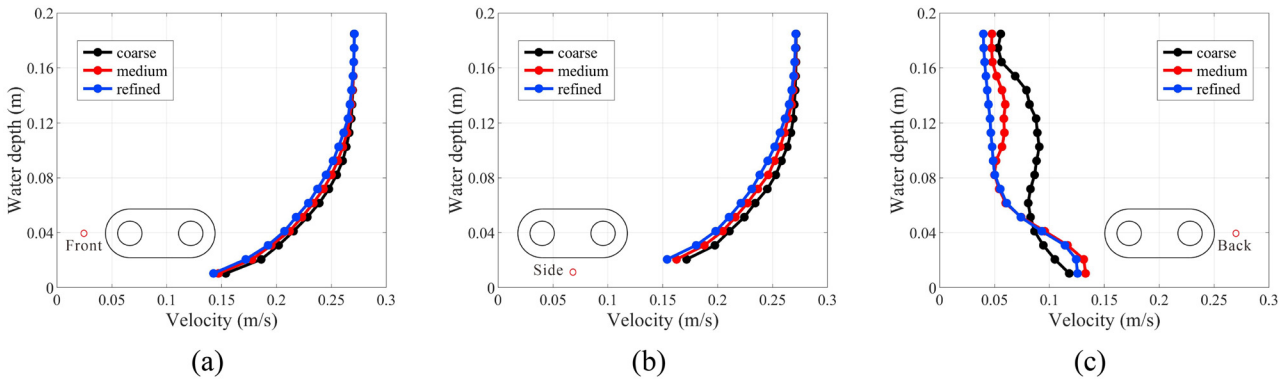

FIG. 14. Comparison of flow velocity profiles for different grid resolutions: (a) front monitoring point, (b) side monitoring point, and (c) back monitoring point.

TABLE III. Grid convergence indices for the flow velocity and TKE.

Key variables	$\delta_{1,2}$	$\delta_{2,3}$	$r_{1,2}$	$r_{2,3}$	m	$GCI_{1,2}$	$GCI_{2,3}$
Velocity	0.0072	0.3997	1.2625	1.2573	12.3683	14.82%	0.049%
TKE	−0.0001	−0.0233	1.2625	1.2573	4.8563	18.39%	1.89%

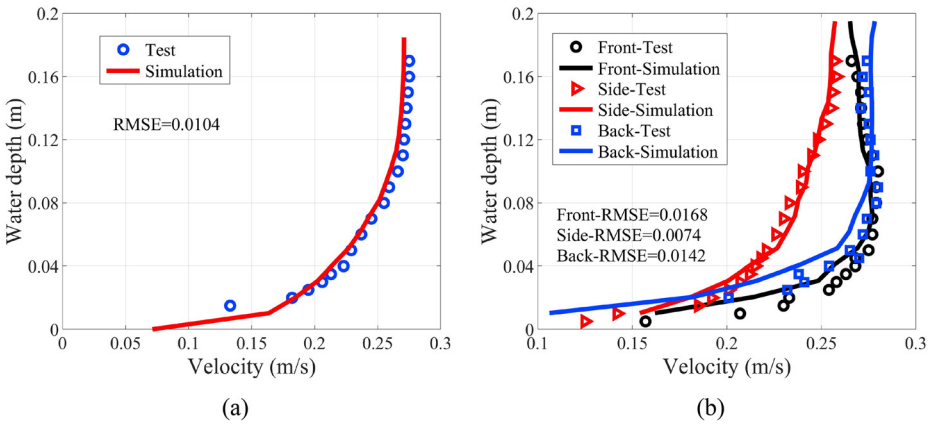

FIG. 15. Comparison of the test and simulated flow velocities of the (a) empty flume and (b) flume with a skirted caisson.

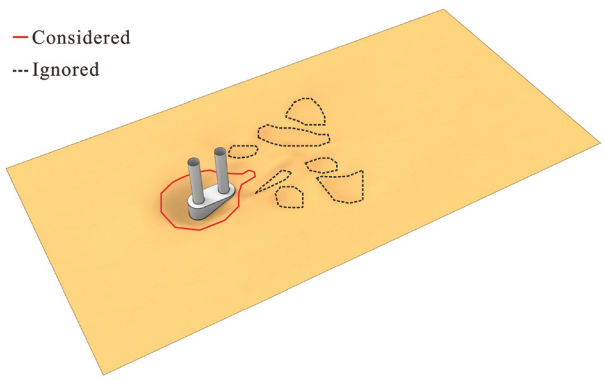

FIG. 16. Calculated ranges of the scour area and volume.

$$f = f_{exact} + g_m j^m + O(j^{m+1}), \tag{6}$$

$$r_{k,k+1} = \frac{j_k}{j_{k+1}} = \left(\frac{N_{k+1}}{N_k}\right)^{\frac{1}{3}}, \tag{7}$$

$$\delta_{r(k,k+1)} = \left|\frac{f_k - f_{k+1}}{f_{k+1}}\right| = \left|\frac{\delta_{k,k+1}}{f_{k+1}}\right|, \tag{8}$$

$$\frac{\delta_{k,k+1}}{r_{k,k+1}^m + 1} = \frac{\delta_{k+1,k+2} r_{k+1,k+2}^m}{r_{k+1,k+2}^m - 1}, \tag{9}$$

$$GCI_{1,2} = F_s \frac{\delta_{r(k,k+1)} r_{k,k+1}^m}{r_{k,k+1}^m - 1}, \quad GCI_{2,3} = F_s \frac{\delta_{r(k,k+1)}}{r_{k,k+1}^m - 1}, \tag{10}$$

where f is the discrete solution, f_{exact} is the exact solution, g_m is the function illustrated in the continuum and does not lean on discretization, j is the grid spacing, m is the order number, k is the kth case, r is

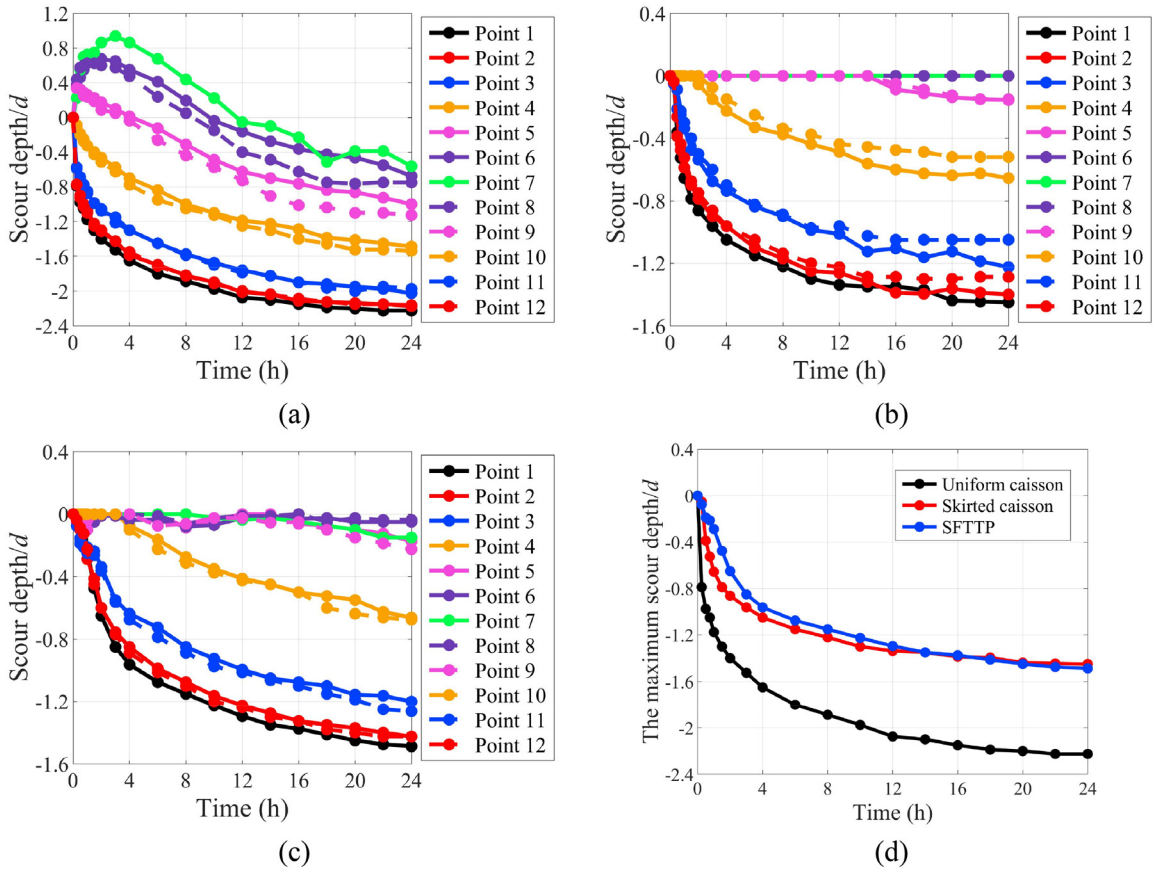

FIG. 17. Temporal development of the scour depth for foundations: (a) uniform foundation, (b) skirted caisson, (c) SCTTP, and (d) the maximum scour depth of foundations with different foundation forms.

the grid refinement ratio, N is the grid number, $\delta_{k,k+1} = f_k - f_{k+1}$, and F_s is the safety factor and equals 1.25 for three different grids.[69] $GCI_{1,2}$ represents the numerical calculation errors between the coarse and medium grids, and $GCI_{2,3}$ represents the numerical calculation errors between the medium and refined grids.

In this section, the velocity and turbulence kinetic energy (TKE) were selected as indicators to calculate the GCI at different grid resolutions. The characteristic point was located in the scour hole. The GCI values are shown in Table III. The GCI for the finer grid $GCI_{2,3}$ is lower than that for the coarser grid $GCI_{1,2}$, which implies that the dependency of the numerical simulation on the cell size has been reduced. In addition, $GCI_{2,3}$ is less than 3% for both the velocity and TKE, indicating that a medium grid resolution is acceptable for numerical simulations.[70] Therefore, the total grid number was set to 1 million in this study. Notably, the number of grids is slightly different due to the different models.

The details of mesh generation are as follows: (1) Setting the face grid size: The global face grid size was set between 5 and 50 mm. Finer grids, ranging from 5 to 10 mm, were applied around the SCTTP and riverbed. (2) Generating and controlling the face grid quality: The face grid was generated according to the specified sizes. The grid quality was controlled by ensuring that the maximum skewness did not exceed 0.7. (3) Setting the boundary layer grid size and generating the volume grid: The boundary layer grid grew on the wall boundary, with its size determined by the aspect ratio. The first aspect ratio was set to 10, the number of layers was set to 5, and the growth rate was set to 1.2. The polygrid form was selected to generate the volume grid. (4) Controlling the volume grid quality: The volume grid quality was maintained by adjusting the nodes to ensure that the maximum skewness remained below 0.7.

D. Validation of the numerical flume

In this section, the flow velocity profiles of the numerical flume were validated in an empty flume and a flume with model #2 under no sediment conditions. In the empty numerical flume, a vertical monitoring line is set in the position of the installed model to obtain the simulated velocity profile. In the numerical flume with the model, three vertical monitoring lines are set in front, side, and back of the skirted caisson model [at distances of $-2.5(l + D)$, $-3.25\,D$, and $2.5\,l + D$ from the model center]. The velocity profiles of the numerical simulation and the test are compared in Fig. 15. The corresponding root mean square errors (RMSEs) are also shown in Fig. 15. It is clear that the simulated flow agrees with the test results for both the empty

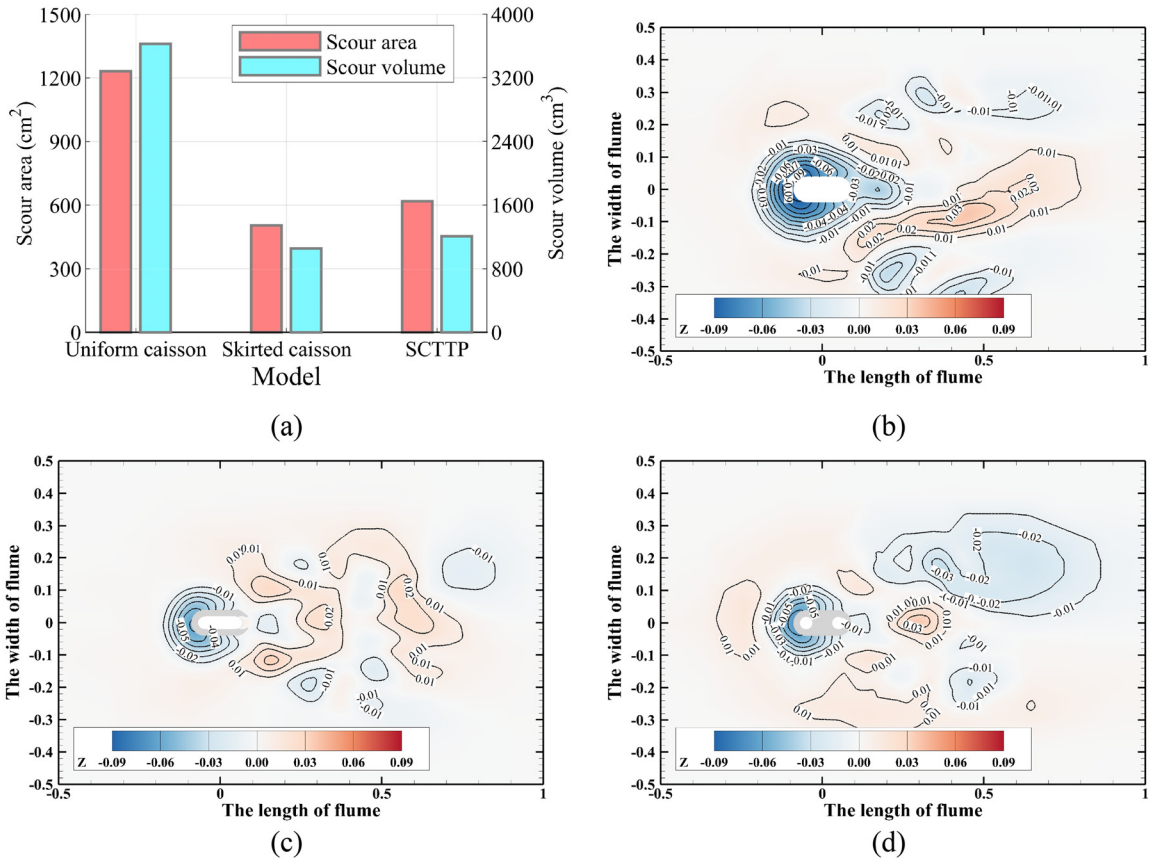

FIG. 18. Scour for foundations at the moment of 24-h scour: (a) scour area and volume, (b) scour terrain of the uniform caisson, (c) scour terrain of the skirted caisson, and (d) scour terrain of the SCTTP.

flume and the flume with the skirted caisson model, and the corresponding RMSEs are small. The validation confirmed that the simulation precision of the flow field in the flume was acceptable. Therefore, numerical simulations of the flow field around the model with the scour terrain were carried out for all nine testing cases.

IV. RESULTS AND DISCUSSION

This section summarizes the experimental and numerical results for the scour of nine models and discusses the effects of the foundation form, the cross-sectional shape of the pier, the distance between two piers and the width of the tie beam on the temporal development law and mechanism of local scour from the perspectives of scour depth development, 24-h scour area, and volume, flow streamlines, vortices, and shear.

The skirt was level with the riverbed, and the rulers on the pier recorded the siltation height. However, siltation above the skirt occurred in a few cases, and the range and height were limited. Therefore, this study mainly focused on the scour of the skirt portion, and the siltation height on the skirt was treated as 0. Certainly, the siltation was discussed, but it was not displayed in the figures.

When calculating the scour area and volume, only the scour around the foundation was considered, and the riverbed scour behind the foundation was not considered, as shown in Fig. 16.

The third vortex identification method, Liutex Omega, was used to evaluate the vorticity. Compared with the first and second vortex identification methods, the third vortex identification method can represent, display, and measure the vortex correctly and identify the six essential elements of the vortex, which overcomes the shortcomings of the first and second vortex identification methods.[71,72] The calculation method is expressed by the following equations:

$$\tilde{\Omega}_R = \frac{(\boldsymbol{\omega}\cdot\mathbf{r})^2}{2[(\boldsymbol{\omega}\cdot\mathbf{r})^2 - 2\lambda_{ci}^2 + 2\lambda_{cr}^2 + \lambda_r^2] + \varepsilon}, \tag{11}$$

where $\tilde{\Omega}_R$ is the relative strength of the vortex, $\boldsymbol{\omega}$ is the vorticity vector ($\nabla \times \boldsymbol{v}$), $\boldsymbol{v}$ is the velocity vector, $\mathbf{r}$ is the Liutex direction vector (real eigenvector of the velocity gradient tensor matrix), and λ_{ci}, λ_{cr}, and λ_r are the imaginary part, the real part of the complex eigenvalue, and the real eigenvalue of the velocity gradient tensor matrix, respectively,

$$\varepsilon = b_0(\beta^2 - \alpha^2)_{\max}, \tag{12}$$

in which the range of b_0 is from 0.001 to 0.002, $\beta = 0.5\boldsymbol{\omega}\cdot\mathbf{r}$, and $\alpha = 0.5\sqrt{(\boldsymbol{\omega}\times\mathbf{r})^2 - 4\lambda_{ci}^2}$.

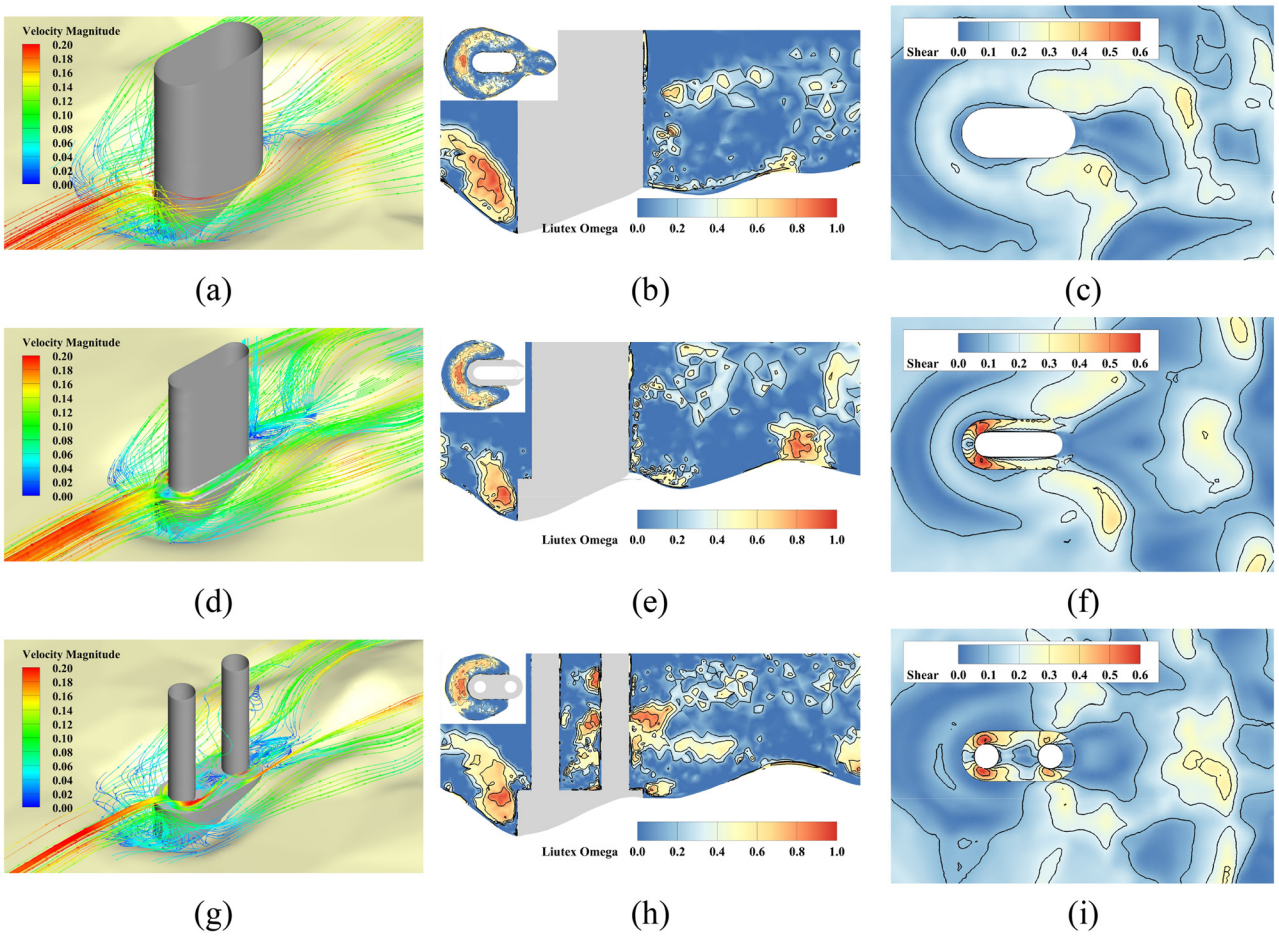

FIG. 19. The flow field for foundations: (a) streamline of uniform caisson (m/s), (b) vortex of uniform caisson, (c) shear of uniform caisson (Pa), (d) streamline of skirted caisson (m/s), (e) vortex of skirted caisson, (f) shear of skirted caisson (Pa), (g) streamline of SCTTP (m/s), (h) vortex of SCTTP, and (i) shear of SCTTP (Pa).

A. Effect of the foundation form on local scour

This section investigated the effects of foundation form on local scour, including three models: uniform caisson (model #1), skirted caisson (model #2), and SCTTP (model #3).

During the test, the scour depth of the monitoring points at different times was recorded. The temporal development of the scour depth of the different foundation forms is shown in Figs. 17(a)–17(c). The scour depth gradually decreases from the front to the back of the foundation for all the cases. The scour of uniform caisson develops rapidly due to the large water-blocking width and the lack of anti-scour countermeasures. During the initial period, scour occurred at the front of the caisson, and the scoured sediment was transported to the back of the caisson, resulting in siltation, which can be observed at points 6–8 in Fig. 17(a). However, as the scour continued, the area around the caisson gradually turned into the scour zone, and the scour depth increased. For the skirted caisson and SCTTP, scour first occurred at points 2 and 12 during the initial period, after which the scour gradually extended to the front of the foundation. The scour groove was connected at point 1 because scour did not occur at point 1, and the scour depth at points 2 and 12 increased gradually during the initial period (approximately the first half hour), as shown in Figs. 17(b) and 17(c). Additionally, the sediment of the initial scour was gradually transported backward, and siltation occurred at the middle of the foundation (points 4 and 10), which is different from a uniform caisson. This is why points 4 and 10 had horizontal segments, as shown in Figs. 17(b) and 17(c). The scour depth of the front and middle of the foundation increased with time for the skirted caisson and SCTTP. However, the scour at the back of the foundation differed between the skirted caisson and the SCTTP. The skirted caisson had siltation (0.2–0.43 d) above the back end of the skirt throughout the test, which is not shown in Fig. 17(b), as previously mentioned. The scour at the back of SCTTP experienced a process of decreasing, as shown in Fig. 17(c). The reason is that the scoured sediment in front of the SCTTP was transported to the position of the initial scour hole at the back of the SCTTP, which caused the scour depth to decrease. Figure 17(d) shows the temporal development of the maximum scour depth of the different foundation forms. In the initial period, the scour development rate of the SCTTP was

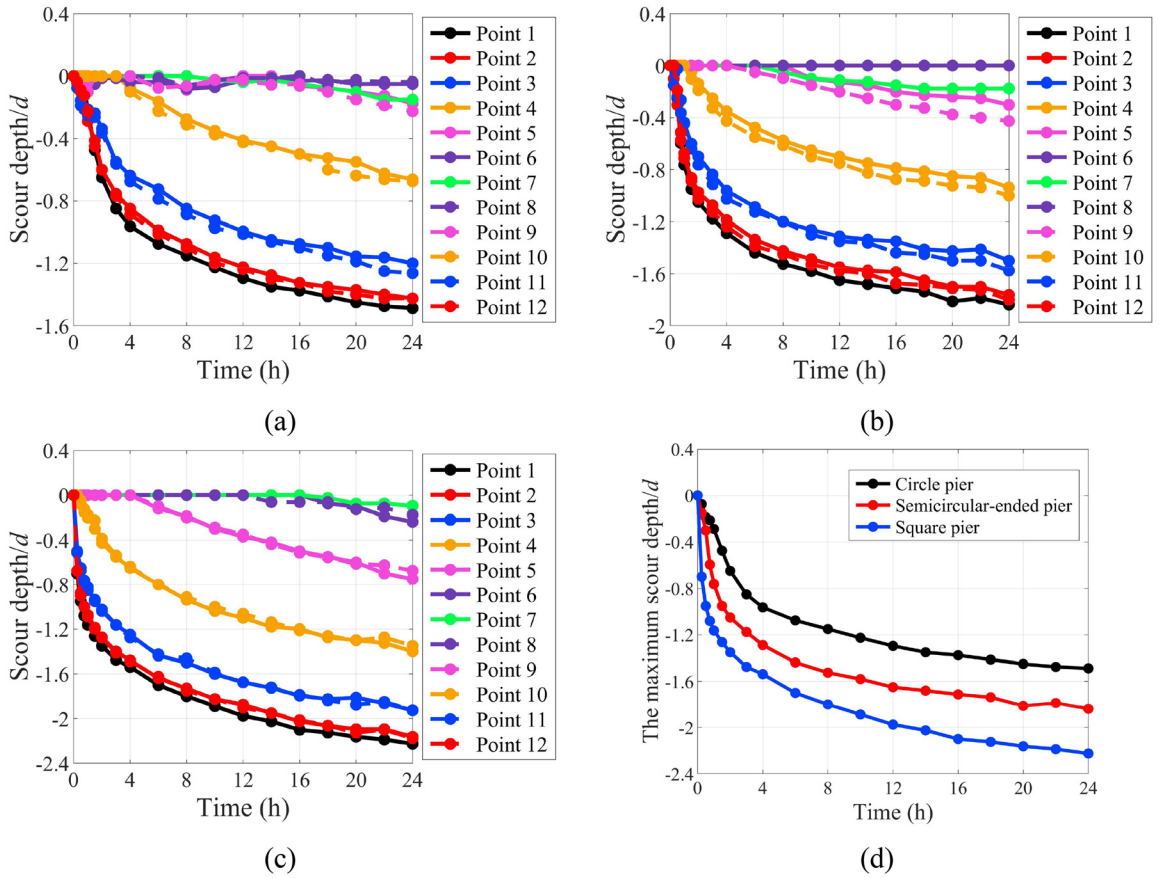

FIG. 20. Temporal development of the scour depth for the SCTTPs: (a) circular pier, (b) semicircular-ended pier, (c) square pier, and (d) maximum scour depth of the SCTTP with different cross-sectional shapes of the pier.

the smallest, and that of the uniform caisson was the largest. At the moment of 24-h scour, the maximum scour depths of the skirted caisson and SCTTP were close, 0.65 and 0.67 times greater than that of the uniform caisson, respectively.

After the test, the scour terrain was collected using oblique photogrammetry technology. The scour area and volume for different foundation forms are shown in Fig. 18(a). The scour area and volume of the uniform caisson are much larger than those of the skirted caisson and SCTTP. The scour areas of the uniform caisson are 2.45 times and 1.99 times greater than those of the skirted caisson and SCTTP, respectively, and the scour volumes of the uniform caisson are 3.45 times and 3.01 times greater than those of the skirted caisson and SCTTP, respectively. A large water-blocking width and lack of anti-scour countermeasures cause a large scour area and depth, as shown in Fig. 17(b), and indirectly lead to a large scour volume. In addition, the scour zone completely encloses the uniform caisson. Compared with those of the uniform caisson, owing to the protection of the skirt and the small water-blocking width of the upper part of the skirted caisson and SCTTP, the scour zones of the skirted caisson and SCTTP are smaller. For the skirted caisson, there is a certain siltation above the back of the skirt, as shown in Fig. 18(c). Therefore, the calculated scour area does not cover the entire skirted caisson. The scour zone of the SCTTP is larger than that of the skirted caisson due to the scour at the back of the SCTTP, and the scour zone nearly encloses the SCTTP, as shown in Fig. 18(d).

The flow fields of different foundation forms under scour terrain conditions are shown in Fig. 19. Unlike the uniform caisson, the skirt of the skirted caisson and the SCTTP stops some of the downward and accelerated flow from impacting and shearing the riverbed, as shown in Figs. 19(a), 19(d), and 19(g). In terms of the vortex, Fig. 19(b), 19(e), and 19(h) provide the front view ($y = 0$ m) and the top view ($z = -0.015$ m) of the Liutex Omega of the different form foundations. Although the scour has continued for 24 h, the range and intensity of the horseshoe vortex of the uniform caisson are still larger than those of the skirted caisson and SCTTP due to the large water-blocking width and lack of anti-scour countermeasures. Compared with a uniform caisson, a skirt plays an essential role in blocking the shear caused by accelerated flow, as shown in Figs. 19(c), 19(f), and 19(i). In addition, the large shear at points 2 and 12 caused the scour to occur first in the initial period at these points, as mentioned above. In addition, there are apparent differences in the shear at the back of the foundation between the skirted caisson and the SCTTP. The shear above the skirt is lower at the back of the skirted caisson. Thus, scour does not develop, and even siltation occurs. However, the shear around the

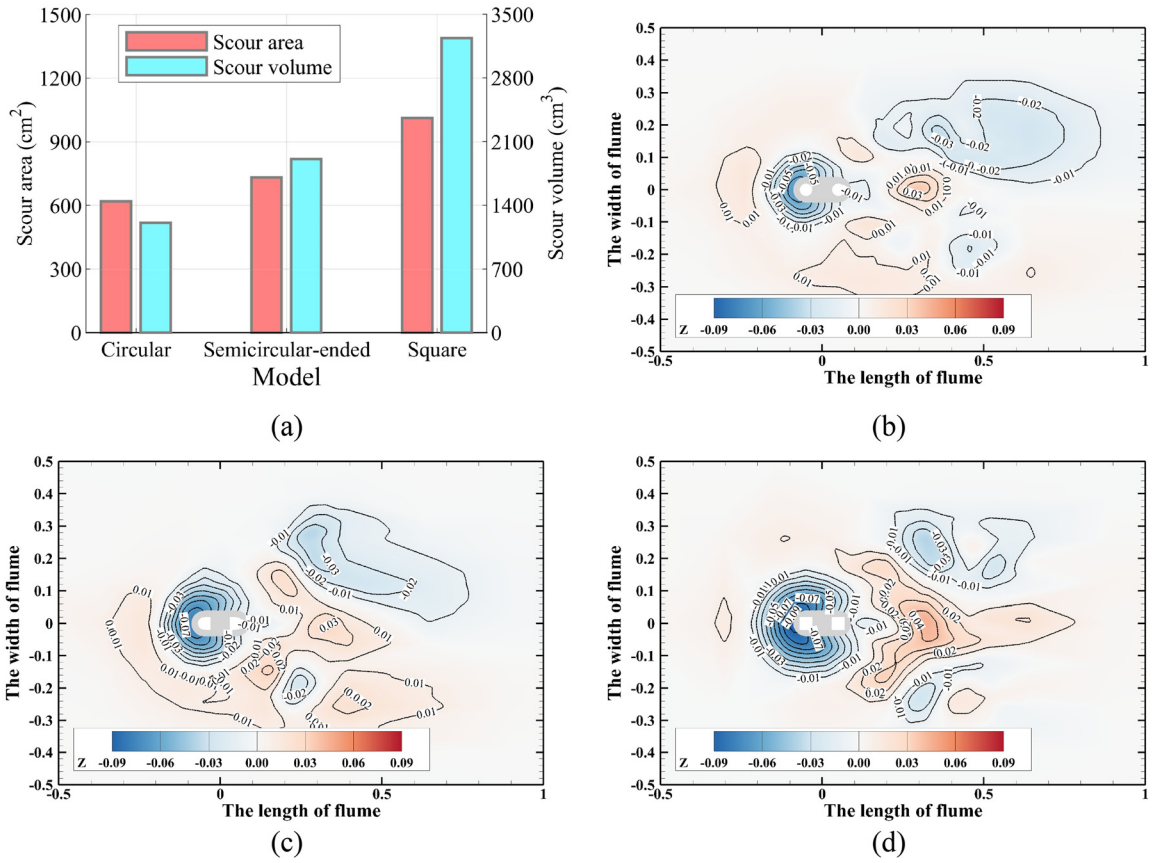

FIG. 21. Scour for SCTTPs at the moment of 24-h scour: (a) scour area and volume, (b) scour terrain of the SCTTP with a circular pier, (c) scour terrain of the SCTTP with a semicircular-ended pier, and (d) scour terrain of the SCTTP with a square pier.

back pier of the SCTTP is greater, which drives the scour to develop continually. Therefore, the scour area of the SCTTP is larger than that of the skirted caisson. Although the scour area of the SCTTP increases, the elevation difference in the riverbed between the front and back of the SCTTP decreases, which reflects that the scour terrain of the SCTTP is more stable.

B. Effect of the cross-sectional shape of the SCTTP pier on local scour

This section investigated the effects of the cross-sectional shape of the SCTTP pier on local scour, including three models: the SCTTP with the circular pier (model #3), the SCTTP with the semicircular-ended pier (model #4), and the SCTTP with the square pier (model #5).

The temporal developments of the scour depth of the different cross-sectional shapes of the SCTTP pier are shown in Figs. 20(a)–20(c). The scour development at the front of SCTTPs with different cross-sectional shapes of the pier is generally the same. The scour develops quickly in the initial period, after which the scour development rate decreases. The scour at the middle and back of the SCTTPs differs due to the different cross-sectional shapes of the pier. In the initial period, the middle of the SCTTPs with semicircular-ended and square piers (points 4 and 10) did not form a horizontal segment, indicating that siltation did not occur. Instead, the horizontal segment is moved to points 5 and 9, which differs from the SCTTP with the circular pier. This is because the back flat surface of the front pier and the front flat surface of the back pier cause the scour to be aggravated in the middle of the two piers. The scoured sediment in the front and middle of the SCTTP is transported together to the back end of the SCTTP. Therefore, the horizontal segment appeared at points 5 and 9. In addition, due to the scour in the middle of the SCTTP, the scour at the front of the SCTTP is not restricted, causing the scour depth to intensify, as shown in Figs. 20(b) and 20(c). In addition, due to the front flat surface of the square pier, the scour of the SCTTP with the square pier is greater than that of the SCTTPs with the circular pier and semicircular-ended pier. Figure 20(d) shows the temporal development of the maximum scour depth of SCTTP with different cross-sectional shapes of the pier. The maximum scour depths of the SCTTP with circular piers, the SCTTP with semicircular-ended piers, and the SCTTP with square piers are distributed from smallest to largest. At the moment of 24-h scour, the maximum scour depths of the SCTTP with the semicircular-ended pier and the square pier are 1.24 and 1.5 times greater than those of the SCTTP with the circular pier, respectively.

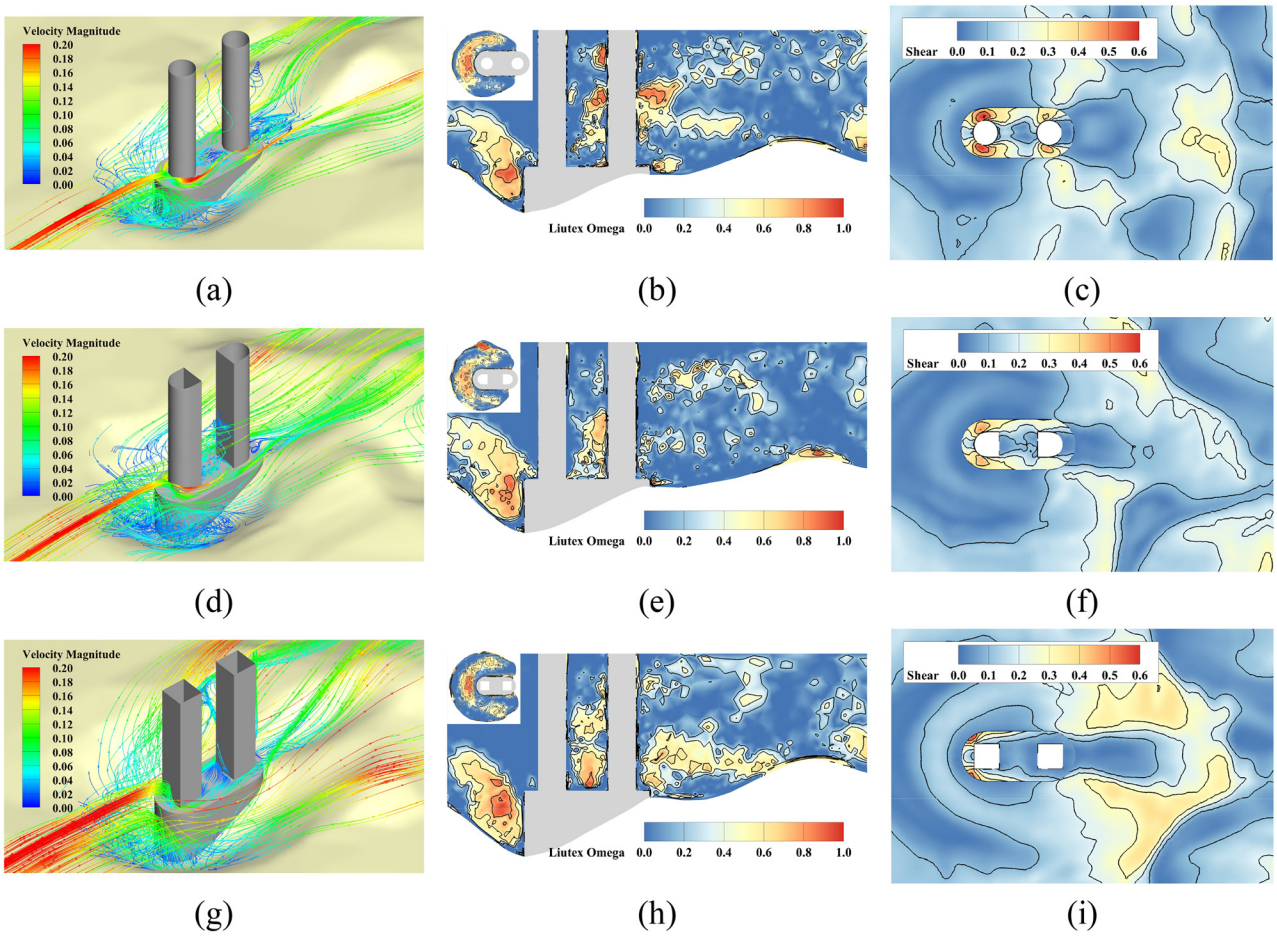

FIG. 22. The flow field for SCTTPs: (a) streamline of SCTTP with circular pier (m/s), (b) vortex of SCTTP with circular pier, (c) shear of SCTTP with circular pier (Pa), (d) streamline of SCTTP with semicircular-ended pier (m/s), (e) vortex of SCTTP with semicircular-ended pier, (f) shear of SCTTP with semicircular-ended pier (Pa), (g) streamline of SCTTP with square pier (m/s), (h) vortex of SCTTP with square pier, and (i) shear of SCTTP with square pier (Pa).

The distributions of the scour area and volume of the SCTTPs with different cross-sectional shapes of the pier are consistent with the maximum scour depth, as shown in Fig. 21(a). The scour areas of SCTTPs with semicircular-ended piers and square piers are 1.19 and 1.64 times greater than those of SCTTPs with circular piers, respectively, and the scour volumes of SCTTPs with semicircular-ended piers and square piers are 1.59 and 2.69 times greater than those of SCTTPs with circular piers, respectively. The contour lines of the SCTTPs with different cross-sectional shapes of the pier are shown in Figs. 21(b)–21(d), and the relative relationships between the scour zone and depth of the SCTTPs with different cross-sectional shapes of the pier are shown. Nearly all of the scour zones of SCTTPs with different cross-sectional shapes of pier enclose the corresponding SCTTPs. The differences are reflected in the scour area and depth of the scour zone of the SCTTP with different cross-sectional shapes. As mentioned above, the flat surfaces of the semicircular-ended pier and square pier indirectly intensify the scour area and depth.

The flow fields of SCTTPs with different cross-sectional shapes of the pier are shown in Fig. 22. The downward flow induced by the arc surface of the circular pier and semicircular-ended pier is weaker than that induced by the flat surface of the square pier, as shown in Figs. 22(a), 22(d), and 22(g), which intensifies the scour of the SCTTP with the square pier. The front view ($y = 0$ m) and the top view ($z = -0.015$ m) of the Liutex Omega of the SCTTP with different cross-sectional shapes of the pier are shown in Figs. 22(b), 22(e), and 22(h). After a 24-h scour, the range and intensity of the horseshoe vortices of the SCTTP with different cross sections of the pier tend to be the same. However, the vortexes between the two piers of the SCTTP with different cross-sectional shapes exhibit specific differences. The intensity of vortexes near the skirt surface between the two piers of the SCTTP with semicircular-ended piers and square piers is greater, which is the reason for the aggravation of scour in the middle of the SCTTPs. According to Figs. 22(c), 22(f), and 22(i), the shear of the riverbed around the caisson is small due to the 24-h scour. However, the initial development of scour can be inferred from the shear on the caisson. The shear at the sides of the two circular piers is greater, and initial scour occurs there. The larger shear only appears on the sides of the front piers for the SCTTP with semicircular-ended pier and square

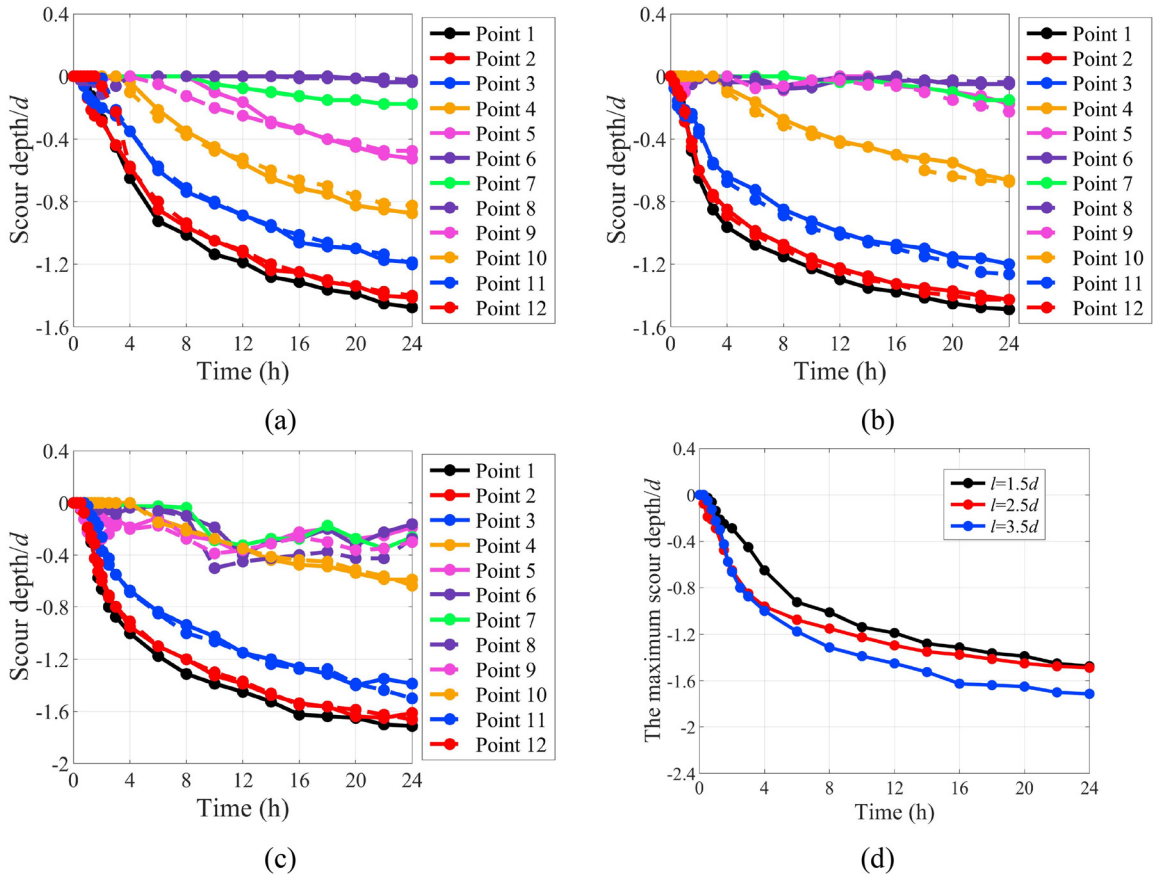

FIG. 23. The temporal development of the scour depth for the SCTTPs: (a) $\boldsymbol{l = 1.5\,d}$, (b) $\boldsymbol{l = 2.5\,d}$, (c) $\boldsymbol{l = 3.5\,d}$, and (d) the maximum scour depth of the SCTTP with different distances between the two piers.

pier because the flat surfaces of the front semicircular-ended pier and the front square pier disperse the flow and prevent the flow from directly impacting the back pier. Therefore, the intensity of accelerated flow is not strong at the back semicircular-ended pier or the back square pier. Additionally, the magnitude of the scour depth of different SCTTPs can be inferred indirectly from the shear range and intensity blocked by the skirt.

C. Effect of the distance between two piers of the SCTTP on local scour

This section investigated the effects of the distance between the two piers of the SCTTP on the local scour, including three models: the SCTTP with $l = 1.5\,d$ (model #6), the SCTTP with $l = 2.5\,d$ (model #3), and the SCTTP with $l = 3.5\,d$ (model #7).

The temporal developments of the scour depth of SCTTPs with different distances between two piers are shown in Figs. 23(a)–23(c). The scour depth gradually decreases from the front to the back of the SCTTP with $l = 1.5\,d$, and the scour depth at 24 h becomes relatively evenly distributed with increasing distance from the front of the SCTTP. With increasing l, a fluctuation in the scour depth occurs around the back of the SCTTP, which does not appear in the SCTTP with $l = 1.5\,d$ and is highly intense in the SCTTP with $l = 3.5\,d$. This is because the influence of the front pier on the back pier decreases with increasing l, and the scour at the front and back of the SCTTP are relatively independent. Therefore, the scour depth at the back of the SCTTP with $l = 3.5\,d$ is greater than those with $l = 1.5\,d$ and $l = 2.5\,d$ in the scour process. Additionally, the scoured sediment at the front of the SCTTP was transported to the middle of the SCTTP, where it formed siltation. The silted sediment continues to be transported to the back of the SCTTP, causing a decrease in the scour depth at the back of the SCTTP. Therefore, a fluctuation in the scour depth occurs around the back of the SCTTP with increasing l. Figure 23(d) shows the temporal development of the maximum scour depth of the SCTTP with different distances between the two piers. The maximum scour depth of the SCTTP with $l = 1.5\,d$ is smaller. However, as the silted sediment in the middle of the SCTTP was transported to the back of the SCTTP, the scour intensified. Therefore, the maximum scour depth of the SCTTP with $l = 1.5\,d$ is close to that with $l = 2.5\,d$. For the SCTTP with $l = 3.5\,d$, the scour at the back of the SCTTP is severe, which intensifies the scour at the front of the SCTTP. Therefore, the maximum scour depth of the SCTTP with $l = 3.5\,d$ is greater than those of the SCTTPs with $l = 1.5\,d$ and $l = 2.5\,d$, roughly by a factor of 1.15.

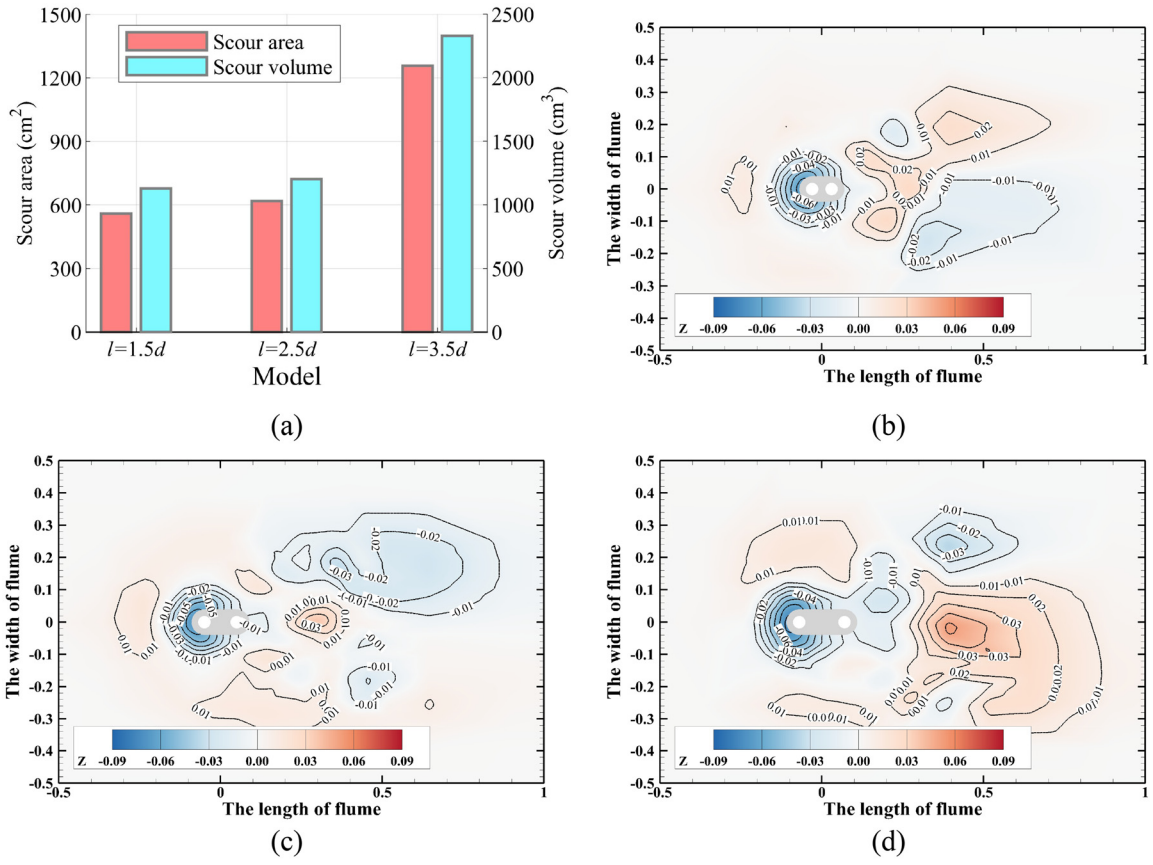

FIG. 24. Scour for SCTTPs at the moment of 24-h scour: (a) scour area and volume, (b) scour terrain of SCTTP with $\boldsymbol{l} = 1.5\,\boldsymbol{d}$, (c) scour terrain of SCTTP with $\boldsymbol{l} = 2.5\,\boldsymbol{d}$, and (d) scour terrain of SCTTP with $\boldsymbol{l} = 3.5\,\boldsymbol{d}$.

The scour area and volume for SCTTPs with different distances between two piers are shown in Fig. 24(a). The scour area and volume of the SCTTPs with $l = 1.5\,d$ and $l = 2.5\,d$ are roughly the same, whereas those of the SCTTP with $l = 3.5\,d$ are greater. This result is consistent with the maximum scour depth. The scour areas of the SCTTPs with $l = 1.5\,d$ and $l = 3.5\,d$ are 0.91 and 2.03 times greater than those of the SCTTPs with $l = 2.5\,d$, and the scour volumes of the SCTTPs with $l = 1.5\,d$ and $l = 3.5\,d$ are 0.94 and 1.94 times greater than those of the SCTTPs with $l = 2.5\,d$. According to Figs. 24(b)–24(d), the scour at the back of the SCTTP becomes more obvious with increasing l. The scour zone of the SCTTP with $l = 1.5\,d$ is a whole due to the smaller l. With increasing l, shrinkage occurs in the middle of the scour zone, which reflects the difference in the formation of the scour zone between the front and back of the shrinkage. The front scour zone is caused by the combined effect of the two piers, whereas the back scour zone is caused by the back pier. With increasing l, the position of the shrinkage moves forward, the back scour zone increases, and the effect of the back pier on the front scour zone is small, as shown in Fig. 24(d).

The flow fields of SCTTPs with different distances between two piers are shown in Fig. 25. l affects mainly the accelerated flow. The accelerated flow generated by the front pier covers the back pier, causing the accelerated flow of the two piers to merge into one, as shown in Fig. 25(a). With increasing l, accelerated flow is generated on the sides of the two piers, as shown in Figs. 25(d) and 25(g). The front view ($y = 0$) and top view ($z = -0.015$) of the Liutex Omega of SCTTPs with different distances between the two piers are shown in Figs. 25(b), 25(e), and 25(h). Based on the approximate scour depth, the range and intensity of the horseshoe vortex of the SCTTP with $l = 2.5\,d$ are larger than those of the SCTTP with $l = 1.5\,d$. While the scour depth of the SCTTP with $l = 3.5\,d$ is large, both the range and the intensity of the horseshoe vortex decrease. The vortexes between the two piers also reflect the influence of the distance between the two piers on the flow field. The smaller l is, the greater the intensity of the vortex between the two piers. In terms of shear, the shear around the sides of the front pier is greater than that around the sides of the back pier. With increasing l, the shear around the front pier and back pier becomes increasingly independent, as shown in Figs. 25(c), 25(f), and 25(i), which explains why the scour zones at the front and back of the SCTTP become increasingly independent.

D. Effect of the width of the SCTTP tie beam on local scour

This section investigated the effects of the width of the SCTTP tie beam on the local scour, including three models: SCTTP with $b = 2\,d$

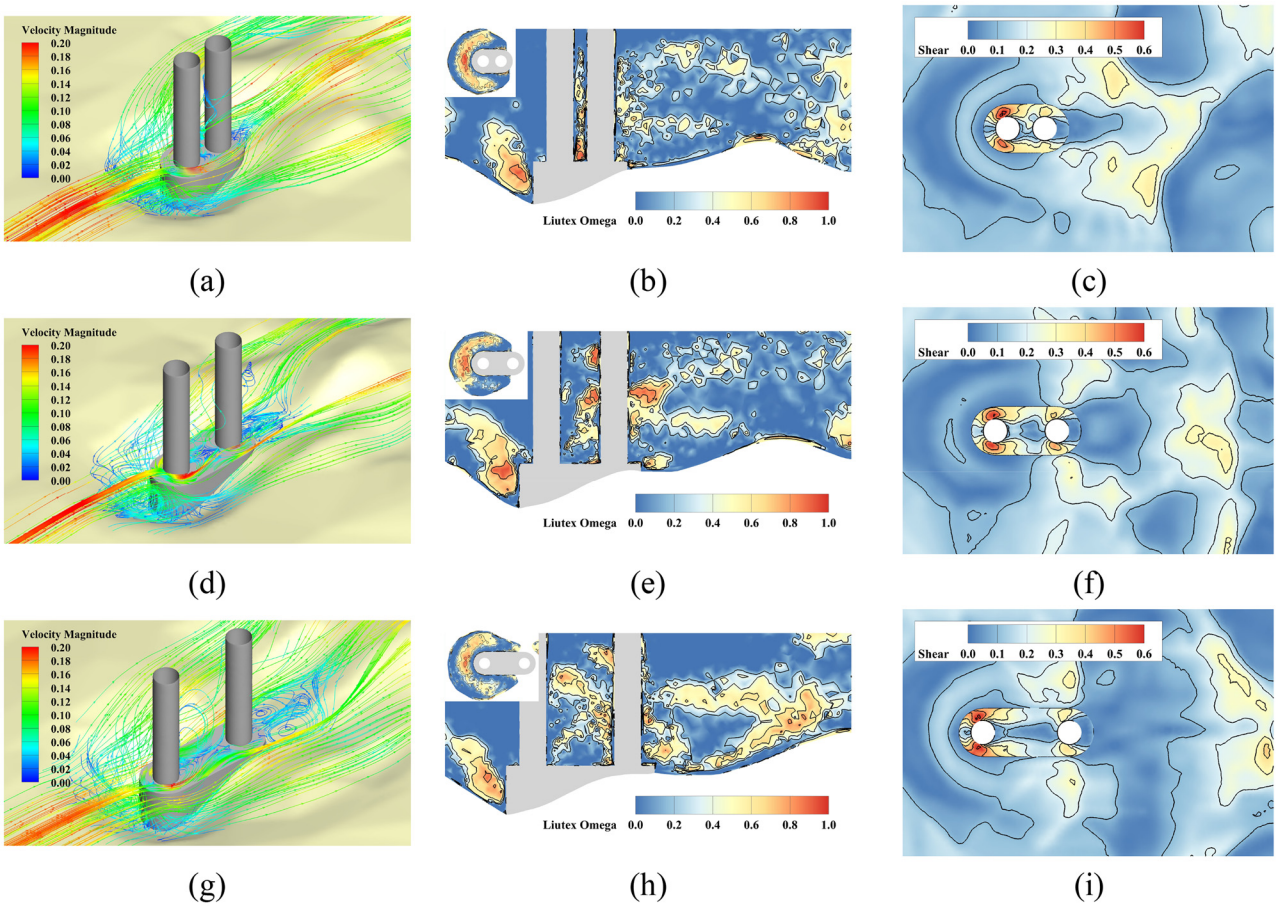

FIG. 25. The flow field for SCTTPs: (a) streamline of SCTTP with $l = 1.5\,d$ (m/s), (b) vortex of SCTTP with $l = 1.5\,d$, (c) shear of SCTTP with $l = 1.5\,d$ (Pa), (d) streamline of SCTTP with $l = 2.5\,d$ (m/s), (e) vortex of SCTTP with $l = 2.5\,d$, (f) shear of SCTTP with $l = 2.5\,d$ (Pa), (g) streamline of SCTTP with $l = 3.5\,d$ (m/s), (h) vortex of SCTTP with $l = 3.5\,d$, and (i) shear of SCTTP with $l = 3.5\,d$ (Pa).

(model #3), SCTTP with $b = 1.5\,d$ (model #8), and SCTTP with $b = d$ (model #9).

The temporal developments of the scour depth of SCTTPs with different widths of tie beam are shown in Figs. 26(a)–26(c). The width of the tie beam decreases, and the skirt is deformed from a round-ended shape to a dumbbell shape. The sudden change in shape in the middle of the skirt aggravated the scour in the middle of the SCTTP. As a result, scour occurs simultaneously in the front and middle of the SCTTPs with $b = 1.5\,d$ and $b = d$ in the initial period, which is different from the SCTTP with $b = 2\,d$. As mentioned above, the scour in the middle of the SCTTP can aggravate the scour in front of the SCTTP. Therefore, the scour depth in front of the SCTTPs with $b = 1.5\,d$ and $b = d$ is greater than that with $b = 2\,d$. In addition, with decreasing b, the depth of the grooves on both sides of the SCTTP increases, causing the scour depth in the middle and back of the SCTTP to increase. Figure 26(d) shows the temporal development of the maximum scour depth of the SCTTP with different widths of the tie beam. The maximum scour depth history curves of the SCTTPs with $b = 1.5\,d$ and $b = d$ almost coincide, which reflects that the maximum scour depth of the SCTTP with a groove in the middle is less affected by the groove depth. Additionally, the maximum scour depth of the SCTTPs with $b = 1.5\,d$ and $b = d$ is 1.34 times greater than that of the SCTTPs with $b = 2\,d$.

The scour area and volume for SCTTPs with different widths of tie beam are shown in Fig. 27(a). The scour area and volume increase with increasing b. The scour zone and volume of the SCTTPs with $b = 1.5\,d$ and $b = d$ are similar, reflecting that the grooves in the middle of the SCTTP play a minor role in the scour area and volume, similar to the law of maximum scour depth. The scour areas of the SCTTPs with $b = 1.5\,d$ and $b = d$ are 1.39 and 1.48 times greater than those of the SCTTPs with $b = 2\,d$, and the scour volumes of the SCTTPs with $b = 1.5\,d$ and $b = d$ are 1.94 and 2.11 times greater than those of the SCTTPs with $b = 2\,d$. According to Figs. 27(b)–27(d), the scour zones enclose the SCTTPs with $b = 1.5\,d$ and $b = d$, whereas the scour zone does not enclose the SCTTP with $b = 2\,d$. Additionally, the difference in the scour zone between SCTTPs with $b = 1.5\,d$ and $b = d$ is mainly at the back of the SCTTP due to the influence of b. The scour zone of the SCTTP with $b = d$ at the back of the SCTTP is relatively large, which makes the elevation difference between the front and the back of the SCTTP relatively small.

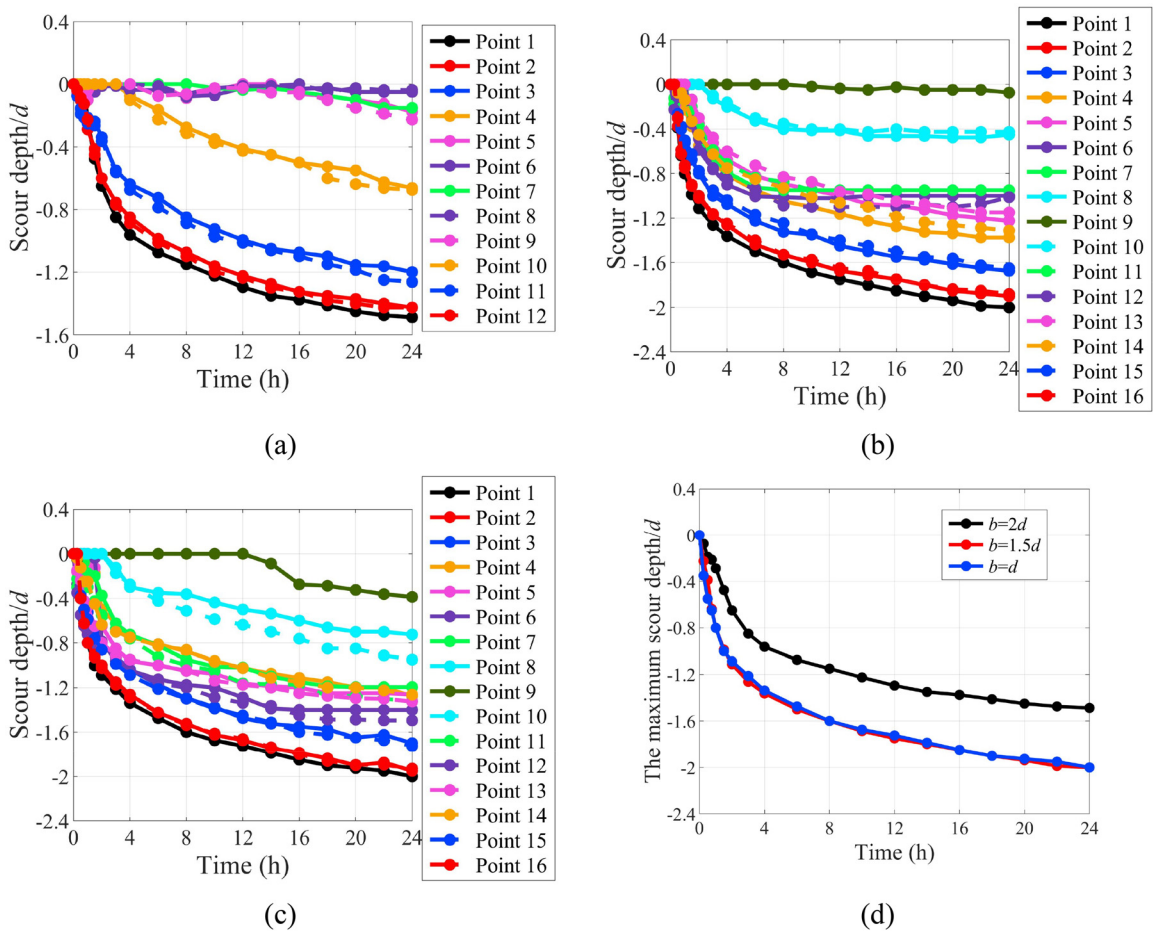

FIG. 26. Temporal development of the scour depth for the SCTTPs: (a) $b = 2\,d$, (b) $b = 1.5\,d$, (c) $b = d$, and (d) the maximum scour depth of SCTTP with different widths of the tie beam.

The flow fields of SCTTPs with different widths of tie beam are shown in Fig. 28. Compared with the smooth tie beam of the SCTTP with $b = 2\,d$, the streamlines at the grooves of the SCTTPs with $b = 1.5\,d$ and $b = d$ are more turbulent, which causes scour to first occur at this position, as shown in Figs. 28(a), 28(d), and 28(g). The front view (y = 0 m) and the top view (z = −0.015 m) of the Liutex Omega of the SCTTP with different widths of tie beam are shown in Figs. 28(b), 28(e), and 28(h). The range and intensity of the horseshoe vortex of the SCTTP with $b = 2\,d$ are greater than those of the SCTTP with $b = 1.5\,d$ and $b = d$ due to the small scour depth. In addition, there are some vortexes at the grooves of the SCTTPs with $b = 1.5\,d$ and $b = d$ according to the top view of the Liutex Omega, which can also explain why scour first occurs in the grooves. In terms of shear, with decreasing b, the shape mutation of the tie beam becomes more obvious, causing the range and intensity of shear around the front pier to increase, as shown in Figs. 28(c), 28(f), and 28(i). Additionally, the shear on the riverbed at the back of the SCTTP with $b = 2\,d$ is greater than that of the SCTTP with $b = 1.5\,d$ and $b = d$, which reflects that the scour at the back of the SCTTPs with $b = 1.5\,d$ and $b = d$ is greater, as shown in the contour line of the terrain.

V. CONCLUSIONS

This study investigated the local scour performance of SCTTPs under steady flow. The effects of the design parameters of the SCTTP, including the foundation form, the cross-sectional shape of the pier, the distance between the two piers, and the width of the tie beam, on the local scour were investigated experimentally and numerically. The temporal development law and mechanism of the local scour of SCTTPs were discussed from the perspective of scour depth development, 24-h scour area and volume, flow streamlines, vortexes, and shear. The main conclusions are as follows:

(1) The skirt plays an essential role in reducing scour due to the blocking effect on the downward and accelerated flows. The maximum scour depths of the skirted caisson and SCTTP are only 0.65 and 0.67 times greater, respectively, than that of the uniform caisson. The scour area and volume of the skirted caisson and SCTTP are smaller than those of the uniform caisson. Because of the more significant shear around the back pier of the SCTTP, the scour at the back of the SCTTP is greater,

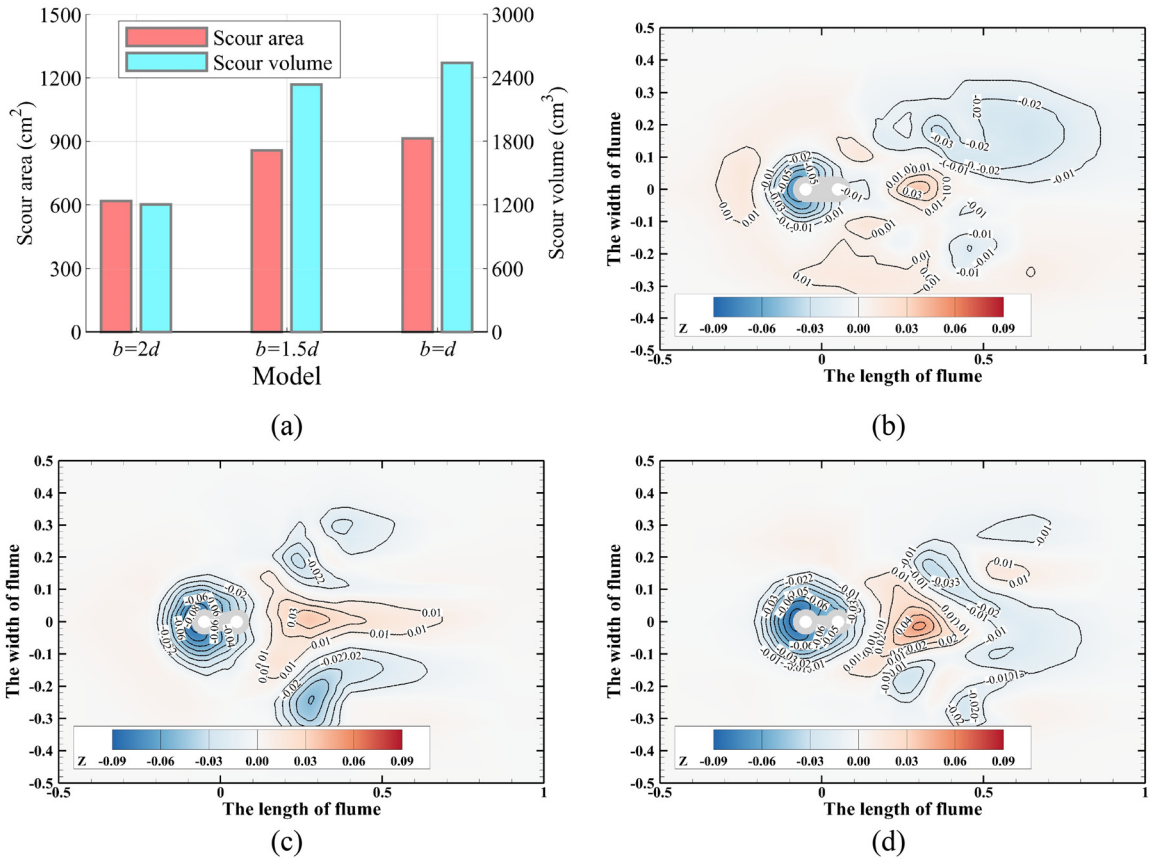

FIG. 27. Scour for SCTTPs at the moment of 24-h scour: (a) scour area and volume, (b) scour terrain of SCTTP with $b = 2\,d$, (c) scour terrain of SCTTP with $b = 1.5\,d$, and (d) scour terrain of SCTTP with $b = d$.

causing the elevation difference in the riverbed between the front and back of the SCTTP to decrease.

(2) For SCTTPs with semicircular-ended piers and square piers, the back flat surface of the front pier and the front flat surface of the back pier enhance the vortex between the two piers, which aggravates the scour in the middle of the SCTTP. The scour at the front of the SCTTP is not restricted, causing the scour depth to intensify. In addition, the front flat surfaces of the front square pier enhance the downward flow, further intensifying the scour of the SCTTP with the square pier. Therefore, the maximum scour depth is ranked as greatest to smallest for the SCTTP with square piers, the SCTTP with semicircular-ended piers, and the SCTTP with circular piers, and the maximum scour depths of the SCTTP with semicircular-ended piers and square piers are 1.24 and 1.5 times greater than those of the SCTTP with circular piers, respectively. The distributions of the scour area and volume of SCTTPs with different cross-sectional shapes of the pier are consistent with the maximum scour depth.

(3) With increasing l, the correlation of the accelerated flow around the piers weakens, the scour at the front and back of the SCTTP gradually becomes independent, and the scour zone at the back of the SCTTPs gradually increases. Due to the intense scour at the back of the SCTTP with $l = 3.5\,d$, the scour at the front of the SCTTP is aggravated. In addition, as the silted sediment in the middle of the SCTTP with $l = 1.5\,d$ was transported to the back of the SCTTP, the scour also intensified. Therefore, the maximum scour depth of the SCTTP with $l = 1.5\,d$ is close to that with $l = 2.5\,d$, and the maximum scour depth of the SCTTP with $l = 3.5\,d$ is more significant than those with $l = 1.5\,d$ and $l = 2.5\,d$, roughly by a factor of 1.15.

(4) With decreasing b, the skirt is deformed from the round-ended to the dumbbell shape. The appearance of grooves causes turbulent flow and the vortex in the grooves, leading to the dramatic development of scour. The flow field at the back of the SCTTP is affected by the turbulent flow at the grooves, leading to an increase in the scour zone of the SCTTP. Additionally, the scour at the front of the SCTTP is not restricted, increasing the scour depth. However, because of the concavity in the groove, the grooves have little effect on the flow field at the front of the SCTTP. Therefore, the maximum scour depth history curves of the SCTTPs with $b = 1.5\,d$ and $b = d$ almost coincide, and the maximum scour depth of the

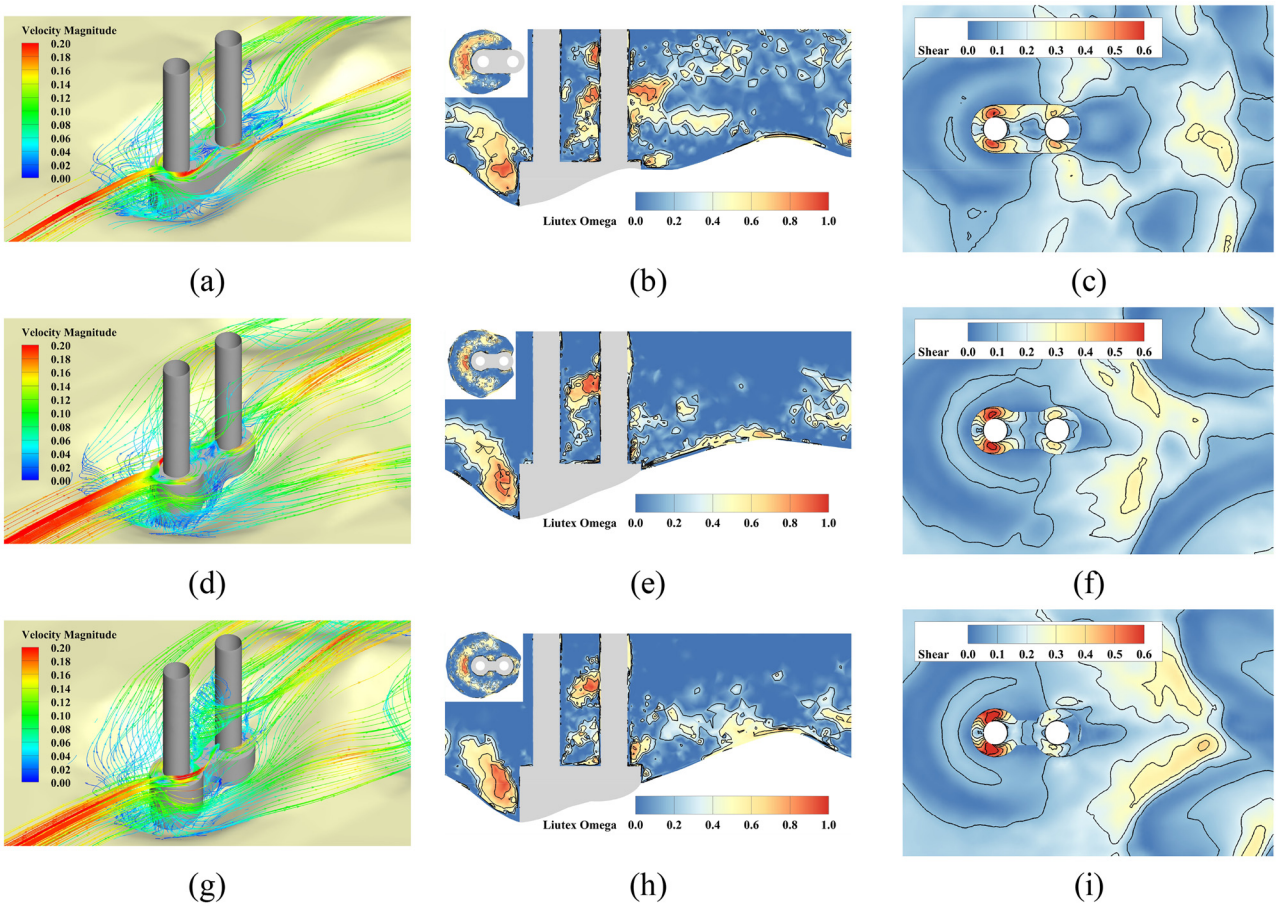

FIG. 28. The flow field for SCTTPs: (a) streamline of SCTTP with $b = 2d$ (m/s), (b) vortex of SCTTP with $b = 2d$, (c) shear of SCTTP with $b = 2d$ (Pa), (d) streamline of SCTTP with $b = 1.5d$ (m/s), (e) vortex of SCTTP with $b = 1.5d$, (f) shear of SCTTP with b=1.5 d (Pa), (g) streamline of SCTTP with $b = d$ (m/s), (h) vortex of SCTTP with $b = d$, and (i) shear of SCTTP with $b = d$ (Pa).

SCTTPs with $b = 1.5d$ and $b = d$ is 1.34 times greater than that of the SCTTP with $b = 2d$.

It should be noted that the testing cases in this paper cannot cover all possible design parameters, such as the cross-sectional shape of the pier, the skirt width, and elevation, which need investigation in the future. The 24-h scour test duration was not long enough to achieve solid equilibrium. Therefore, it is necessary to study the design parameters of the SCTTP on local scour further by carrying out more equilibrium scour tests in the future. Moreover, it is interesting to develop advanced underwater and noncontact terrain measuring techniques to measure the terrain when the scour develops at its intensest, which is more helpful for understanding the scour mechanism. Notwithstanding these limitations, the conclusions drawn from this research provide insight into the engineering design optimization of SCTTPs from the perspective of scour.

ACKNOWLEDGMENTS

The authors would like to acknowledge the National Natural Science Foundation of China (Grant Nos. U21A20154 and 52222804).

AUTHOR DECLARATIONS

Conflict of Interest

The authors have no conflicts to disclose.

Author Contributions

Fang Qiu: Data curation (equal); Investigation (equal); Methodology (equal); Resources (equal); Writing – original draft (equal). **Kai Wei:** Conceptualization (equal); Supervision (equal); Writing – review & editing (equal). **Ke Tong:** Investigation (equal); Validation (equal). **Zhenchen Hu:** Investigation (equal). **Changrong Yao:** Resources (equal). **Jingxi Qin:** Validation (equal).

DATA AVAILABILITY

The data that support the findings of this investigation are available from the corresponding author upon reasonable request.

REFERENCES

[1]K. Wei, X. Zhong, H. Cai, X. Li, and H. Xiao, "Dynamic response of a sea-crossing cable-stayed suspension bridge under simultaneous wind and

wave loadings induced by a landfall typhoon," Ocean Eng. **293**, 116659 (2024).
[2]W. Zhao, K. Wei, and X. Zhong, "Estimation of breaking wave region based on coupled wave and storm surge simulations of historical typhoons: A case study of Hangzhou Bay," Ocean Eng. **286**, 115596 (2023).
[3]X. Lu, K. Wei, K. Deng, and L. Xu, "Lifetime seismic resilience assessment of a sea-crossing cable-stayed bridge exposed to long-term scour and corrosion," Ocean Eng. **295**, 116990 (2024).
[4]S. Li, H. Xiao, J. Zhang, and Y. Bie, "Design of central navigation channel bridge of Hangzhou bay sea-crossing railway bridge," Bridge Constr. **53**(2), 29–36 (2023).
[5]J. Liu, H. Xiao, Z. Fu, and Y. Qiu, "Foundation scheme comparison for pylon No. 5 of Xihoumen rail-cum-road bridge," Bridge Constr. **50**(2), 16–22 (2020).
[6]N. Li, L. Tian, and S. Zhou, "Hydrological monitoring and data analysis of the engineering reach during the construction of Hutong Yangtze River Bridge," Water Resourc. Inf. **40**(6), 43–48 (2022).
[7]Y. Yang, B. W. Melville, G. H. Macky, and A. Y. Shamseldin, "Experimental study on local scour at complex bridge piers under steady currents with bedform migration," Ocean Eng. **234**, 109329 (2021).
[8]S. Chen, "Study of scouring protection schemes for pier foundation of Donghai bridge," World Bridges **47**(4), 17–21 (2019).
[9]Z. Tang, B. Melville, N. Singhal, A. Shamseldin, J. Zheng, D. Guan, and L. Cheng, "Countermeasures for local scour at offshore wind turbine monopile foundations: A review," Water Sci. Eng. **15**(1), 15–28 (2022).
[10]M. Karimaei Tabarestani and A. R. Zarrati, "Reliability analysis of riprap stability around bridge piers," J. Appl. Water Eng. Res. **7**(1), 79–88 (2019).
[11]Gh. Khademghaeiny, J. Abrishami, A. R. Zarrati, M. Karimae. Tabarestani, and M. Mashahir, "Riprap design at bridge piers with limited scouring," Sci. Iran. **27**(2), 588–595 (2020).
[12]C. Valela, C. N. Whittaker, C. D. Rennie, I. Nistor, and B. W. Melville, "Novel riprap structure for improved bridge pier scour protection," J. Hydraul. Eng. **148**(3), 04022002 (2022).
[13]J. Chen, Y. Qu, and Z. Sun, "Protection mechanisms, countermeasures, assessments and prospects of local scour for cross-sea bridge foundation: A review," Ocean Eng. **288**, 116145 (2023).
[14]S. Pagliara, I. Carnacina, and F. Cigni, "Sills and gabions as countermeasures at bridge pier in presence of debris accumulations," J. Hydraul. Res. **48**(6), 764–774 (2010).
[15]Q. He and J. Qi, "A new technology research for scour protection of offshore wind turbine foundation," Southern Energy Constr. **7**(2), 112–121 (2020).
[16]H. Wang, S. T. Ke, T. G. Wang, A. Kareem, L. Hu, and Y. J. Ge, "Multi-stage typhoon-induced wind effects on offshore wind turbines using a data-driven wind speed field model," Renewable Energy **188**, 765–777 (2022).
[17]M. A. Elngar, N. M. AboulAtta, N. Y. Saad, and D. A. El-Molla, "Effect of sacrificial piles on local scour around complex bridge piers," Ain Shams Eng. J. **15**(2), 102410 (2024).
[18]K. Wei, P. Ran, F. Qiu, and J. Hong, "Experimental study on the influence of sacrificial pile section characteristics on the local scour of cylindrical pier," J. Civil Environ. Eng. **46**(5), 152–159 (2023).
[19]H. Kassem, A. A. El-Masry, and R. Diab, "Influence of collar's shape on scour hole geometry at circular pier," Ocean Eng. **287**, 115791 (2023).
[20]Z. Tang, B. Melville, A. Shamseldin, D. Guan, N. Singhal, and Z. Yao, "Experimental study of collar protection for local scour reduction around offshore wind turbine monopile foundations," Coastal Eng. **183**, 104324 (2023).
[21]C. A. Chooplou, M. Vaghefi, and M. Akbari, "Effect of repositioned submerged vanes on local scour variations around a pier in a bend: Experimental investigation," Int. J. Environ. Sci. Technol. **20**(8), 8627–8640 (2023).
[22]M. Vaghefi, E. Zarei, G. Ahmadi, and A. M. Behroozi, "Experimental analysis of submerged vanes' configuration for mitigating local scour at piers in a sharp bend: Influence of quantity, length, and orientation," Ocean Eng. **289**, 116267 (2023).
[23]M. Esmaeili Varaki, N. Tavazo, and A. Radice, "Using a bed sill as a countermeasure for clear-water scour at a complex pier with inclined columns footed on capped piles," Hydrology **9**(4), 65 (2022).
[24]E. Gerami, M. Heidarpour, and R. M. Ghalati, "Effect of simultaneous use of cable and bed sill scour countermeasures around a cylindrical pier," Proc. Inst. Civil Eng. **176**(6), 277–290 (2023).
[25]S. Qin, G. Tan, Q. Lu, Z. Fu, M. Guo, and K. Wei, "Research on design and sinking methods for super large caisson foundation," Bridge Constr. **50**(5), 1–9 (2020).
[26]K. Wei, F. Qiu, and S. Qin, "Experimental and numerical investigation into effect of skirted caisson on local scour around the large-scale bridge foundation," Ocean Eng. **250**, 111052 (2022).
[27]H. Xu, J. Yan, Y. Sun, Y. Wen, and H. Zhang, "Study of influence of setting stepped caisson on hydrodynamic property of surrounding water and local scour," World Bridges **50**(2), 64–70 (2022).
[28]Y. Hu, "Research on pylon foundation types for main navigational channel bridge of Changtai Changjiang River Bridge," Bridge Constr. **51**(2), 1–9 (2021).
[29]K. Wei, D. Shang, and X. Zhong, "Life-cycle thinking-based decision support framework for multispan simply supported bridges under typhoon-induced wave, current and surge conditions," Ocean Eng. **288**, 115965 (2023).
[30]J. A. Sharp and T. O. McAlpin, "Case study: Experimental investigation into the feasibility of pier nose extensions to reduce local scour around bridge piers," J. Hydraul. Eng. **148**(1), 05021010 (2022).
[31]Y. Li, Z. Guo, L. Wang, H. Yang, Y. Li, and J. Zhu, "An innovative eco-friendly method for scour protection around monopile foundation," Appl. Ocean Res. **123**, 103177 (2022).
[32]H. Li, X. Qiu, S. Yan, H. Zhao, and W. Ma, "Numerical investigation on the influence of a spoiler structure for local scour protection," Appl. Ocean Res. **138**, 103675 (2023).
[33]D. Guan, Y. Xie, Y. Chiew, F. Ding, T. F. Ferradosa, and J. Hong, "Estimation of local scour around monopile foundations for offshore structures using machine learning models," Ocean Eng. **296**, 116951 (2024).
[34]C. Wang, Q. Wu, H. Zhang, and F. Liang, "Effect of scour remediation by solidified soil on lateral response of monopile supporting offshore wind turbines using numerical model," Appl. Ocean Res. **150**, 104143 (2024).
[35]A. Barrie, C. Wang, F. Liang, and W. Qi, "Experimental investigation on the mechanism of local scour around a cylindrical coastal pile foundation considering sloping bed conditions," Ocean Eng. **312**, 119225 (2024).
[36]H. Wang, H. Tang, Q. Liu, and Y. Wang, "Local scouring around twin bridge piers in open-channel flows," J. Hydraul. Eng. **142**(9), 06016008 (2016).
[37]P. Yu, J. Liu, L. Yu, and L. Zhu, "Numerical investigation of local scour around tandem piers using proposed self-sustaining inlet turbulent boundary conditions," Ocean Eng. **274**, 113987 (2023).
[38]H. Qi, T. Yuan, W. Zou, W. Tian, and J. Li, "Numerical study on local scour reduction around two cylindrical piers arranged in tandem using collars," Water **15**(23), 4079 (2023).
[39]M. Zhao, X. Zhu, L. Cheng, and B. Teng, "Experimental study of local scour around subsea caissons in steady currents," Coastal Eng. **60**, 30–40 (2012).
[40]Q. Xiang, K. Wei, F. Qiu, C. Yao, and Y. Li, "Experimental study of local scour around caissons under unidirectional and tidal currents," Water **12**(3), 640 (2020).
[41]J. Qin, X. Yang, K. Wei, and F. Qiu, "Cross-sectional blockage effect on the drag force of a scaled round-ended pier model under directional flow," Ocean Eng. **264**, 112532 (2022).
[42]B. Wang and J. Wang, "Production and quality analysis of 3d city modeling using oblique photogrametric technology," Urban Geotech. Invest. Surv. **2015**(5), 80–82+85.
[43]G. Yang and M. Wang, "The tilt photographic measuration technique and expectation," Geomatics Spatial Inf. Technol. **39**(1), 13–15 (2016).
[44]Z. Chen, "Research on oblique photogrammetry technology of bridge," M.S. thesis (Chongqing Jiaotong University, 2023).
[45]Y. He, "A three-dimensional modeling study of oblique photogrammetry of drones in the Western Alpine region," M.S. thesis (East China University of Technology, 2022).
[46]Y. Zhou, "Local scour experiment and numerical simulation of circular pier," M.S. thesis (Southwest Jiaotong University, 2022).
[47]C. Yao, Y. Zhou, L. Guo, H. An, and Q. Liu, "A new method of pier scour test surveying and mapping," J. Waterway Harbor **43**(4), 549–554 (2022).
[48]W. Feng, L. Dandan, and C. Qiang, "Discussion on the application of UAV oblique photography in the registration of rural housing and real estate integration," in *IEEE 5th International Conference on Intelligent Transportation Engineering (ICITE)* (IEEE, Beijing, China, 2020), pp. 290–295.

[49]W. Xi, D. Li, and Z. Zhao, "Single tree three-dimensional model construction and impact factor extraction based on oblique photogrammetry," Rev. Int. Contam. Ambiental **35**, 195–201 (2019).
[50]B. Yang, F. Ali, B. Zhou, S. Li, Y. Yu, T. Yang, X. Liu, Z. Liang, and K. Zhang, "A novel approach of efficient 3D reconstruction for real scene using unmanned aerial vehicle oblique photogrammetry with five cameras," Comput. Electr. Eng. **99**, 107804 (2022).
[51]X. Zhang, P. Zhao, Q. Hu, M. Ai, D. Hu, and J. Li, "A UAV-based panoramic oblique photogrammetry (POP) approach using spherical projection," ISPRS J. Photogramm. Remote Sens. **159**, 198–219 (2020).
[52]B. W. Melville, "Pier and abutment scour: Integrated approach," J. Hydraul. Eng. **123**(2), 125–136 (1997).
[53]S. Jing, W. Yang, and Y. Chen, "Study on characteristics of secondary flows in smooth rectangular open channel," J. Hydroelectr. Eng. **39**(1), 12–20 (2020).
[54]E. V. Richardson and S. R. Davis, *Evaluating Scour at Bridges* (Federal Highway Administration, Washington, DC, 2001).
[55]M. Qi, J. Li, and Q. Chen, "Comparison of existing equations for local scour at bridge piers: Parameter influence and validation," Nat. Hazards **82**(3), 2089–2105 (2016).
[56]D. A. Baghbadorani, A. M. foundation of, A. Beheshti, and B. A. Ashtiani, "Scour hole depth prediction around pile groups: Review, comparison of existing methods, and proposition of a new approach," Nat. Hazards **88**, 977 (2017).
[57]B. W. Melville and Y.-M. Chiew, "Time scale for local scour at bridge piers," J. Hydraul. Eng. **125**(1), 59–65 (1999).
[58]M. F. Mia and H. Nago, "Design method of time-dependent local scour at circular bridge pier," J. Hydraul. Eng. **129**(6), 420–427 (2003).
[59]A. H. Cardoso and R. Bettess, "Effects of time and channel geometry on scour at bridge abutments," J. Hydraul. Eng. **125**(4), 388–399 (1999).
[60]M. Pandey, P. K. Sharma, Z. Ahmad, and U. K. Singh, "Evaluation of existing equations for temporal scour depth around circular bridge piers," Environ. Fluid Mech. **17**(5), 981–995 (2017).
[61]S. Wang, W. Qi, B. Li, Z. Wang, and F. Gao, "Extrapolating time development curves of clear-water scour around piles: From empirical fitting to physics-based approach," Ocean Eng. **306**, 117963 (2024).
[62]D. M. Sheppard and W. Miller, "Live-bed local pier scour experiments," J. Hydraul. Eng. **132**(7), 635–642 (2006).
[63]Y. Yang, B. W. Melville, G. H. Macky, and A. Y. Shamseldin, "Temporal evolution of clear-water local scour at aligned and skewed complex bridge piers," J. Hydraul. Eng. **146**(4), 04020026 (2020).
[64]D. Liang, J. Huang, J. Zhang, S. Shi, N. Zhu, and J. Chen, "Three-dimensional simulations of scour around pipelines of finite lengths," J. Mar. Sci. Eng. **10**(10), 106 (2022).
[65]D. Li, G. Dai, X. Jin, Y. Zeng, and L. Qi, "Research and application of three -dimensional numerical model of local scour based on finite volume method," Chin. J. Comput. Mech. **37**(3), 332–339 (2020).
[66]P. Ran, K. Wei, B. Zhang, L. Wang, R. Nie, and Y. Li, "Experimental and numerical investigation into the local scour of bridge cofferdam with anti-scour ribs," Adv. Bridge Eng. **5**(1), 10 (2024).
[67]Z. He, K. Zhang, G. Wang, and J. Tu, "Vortex-induced vibration of the variable cross-sectional cylinder cases in transverse direction at $Re = 3900$ using OpenFOAM," Ocean Eng. **303**, 117511 (2024).
[68]M. S. Karaalioglu and S. Bal, "Performance prediction of cavitating marine current turbine by BEMT based on CFD," Ocean Eng. **255**, 111221 (2022).
[69]P. J. Roache, "Quantification of uncertainty in computational fluid dynamics," Annu. Rev. Fluid Mech. **29**(1), 123–160 (1997).
[70]S. R. Lizarose Samion, N. H. Shaharuddin, and M. S. Mat Ali, "Grid convergence study for detached-eddy simulation of flow over rod-airfoil configuration using OpenFOAM," IOP Conf. Ser. **491**, 012023 (2019).
[71]C. Liu, "Liutex-third generation of vortex definition and identification methods," Acta Aerodyn. Sin. **38**(3), 413–431+478 (2020).
[72]C. Liu and Y. Yu, "Mathematical foundation of Liutex theory," J. Hydrodyn. **34**(6), 981–993 (2022).